UNIVERSITAT POLITÈCNICA DE BARCELONATECH
Escola Superior d'Engin
Aeroespacial i Audiovisu

Implementation of an attitude control board for CubeSat on one axis with inertial wheel activated by brushless motor.

BACHELOR FINAL THESIS

Document:

Report

Author

Isai Serrano Ramón

Director/Co-director:

Gago Barrio, Javier / Lamich Arocas, Manuel

Degree:

Bachelor in Industrial Technology Engineering

Examination session:

Spring 2023

Abstract

The following work belongs to the PLATHON project (PLATform of integrated simulation of Hardwar in the loop for Optical communications in Nanosatellites), conducted by the research group led by Dr. Javier Gago and Dr. David González at the Polytechnic University of Catalonia in Terrassa, ESEIAAT (Superior School of Industrial, Audiovisual, and Aeronautical Engineering of Terrassa).

The main objective of PLATHON is to replicate a network system composed of CubeSats, which collect data and establish communication with various satellites in orbit. The project heavily relies on the participation of final-year undergraduate and master's degree students from different departments, who contribute significantly to its development.

Specifically, this project consists of developing a method to obtain attitude control of the CubeSat using reaction wheels, with performance similar to commercial solutions. In addition to cost reduction, certain aspects will also be improved or adapted for the final implementation in the CubeSat.

The methodology followed by this project is based on the research and application of theoretical statements for the operation of BLDC motors. Moreover, having access to the UPC facilities in Terrassa has allowed us to experience each situation in the laboratory and make informed decisions.

Finally, the achieved result is a closed-loop voltage control that allows a range of motor speeds and depends on the input voltage. Furthermore, a printed circuit board has been developed to apply a sensing method based on Hall effect sensors.

On the other hand, there have been some limitations, all of which are due to the small size of the BLDC motor used, a characteristic that has influenced most of the project's decisions. Nevertheless, this project can be used as a research foundation or as a starting point for other projects.

Resumen

El siguiente trabajo pertenece al proyecto PLATHON (PLATforma de simulación integrada de Hardwar en bucle para comunicaciones ópticas en Nanosatélites), llevado a cabo por el grupo de investigación liderado por el Dr. Javier Gago y el Dr. David González en la Universitat Politècnica de Catalunya de Terrassa, ESEIAAT (Escuela Superior de Ingenierías Industrial, Audiovisual y Aeronáutica de Terrassa).

El objetivo principal de PLATHON es replicar un sistema de red compuesto por CubeSats, que recopilan datos y establecen comunicación con diversos satélites en órbita. El proyecto depende en gran medida de la participación de estudiantes de último año de grado y máster de diferentes departamentos, quienes contribuyen de manera significativa a su desarrollo.

Específicamente, este proyecto consiste en desarrollar una forma de obtener control de actitud del CubeSat a partir de las ruedas de reacción, con un rendimiento similar a las soluciones comerciales. De esta manera, además de reducir costos, algunos aspectos también se mejorarán o adaptarán para su implementación final en el CubeSat.

La metodología seguida por este proyecto se basa en la investigación y aplicación de declaraciones teóricas para el funcionamiento de motores BLDC. Además, contar con las instalaciones de la UPC en Terrassa nos ha permitido experimentar cada situación en el laboratorio y tomar decisiones basadas en argumentos.

Finalmente, el resultado alcanzado es un control de voltaje en bucle cerrado, que permite un rango de velocidad del motor y depende del voltaje de entrada. Además, se ha desarrollado una placa de circuito impreso para aplicar un método de detección basado en sensores de efecto Hall.

Por otro lado, ha habido algunas limitaciones, todas ellas debido al tamaño reducido del motor BLDC utilizado, una característica que ha condicionado la mayoría de las decisiones del proyecto. Sin embargo, este proyecto puede utilizarse como base de investigación o como punto de partida para otros proyectos.

Contents

List of tables

List of figures

List of abbreviations / Glossary

ADCS	Attitude Determination and Control System.
PWM	Pulse Width Modulation.
LEO	Low Earth Orbit.
PLATHON	PLATform of integrated simulation of Hardwar in the loop for Optical communications in Nanosatellites.
IoT	Internet of Things.
OBC	On Board Computer.
EPS	Electrical Power Supply.
DSBL	Disabled.
DC	Direct Current
BEMF	Back Electro-Motive Force.
PCB	Printed Circuit Board.
IDE	Integrated Development Environment
EDA	Electronic Design Automation
BLDC	Brushless Direct Current
PMSM	Permanent Magnet Synchronous Machine

1 Introduction

1.1 Object

The aim of this project is to redesign an existing attitude control board by replacing the current brushed motor with a brushless one. This change will reduce the issues related to lack of stability and the energy consumption caused by brush friction. In addition to replacing the motor, the power electronics that supply electricity to the motor and the motor driver will need to be changed. Control algorithms also need to be adapted to the new components.

Another motive to make this project is the high price that the previous project cost, considering that a CubeSat would need from three to four motors. For that reason, achieving the same function with less cost is a key objective of this project, distinguishing it from others.

1.2 Scope

To determine the scope of the project, different work packages have been specified. As already mentioned, the project aims to change the motor actuator of the CubeSat in an attempt to reduce its cost. For this goal, the following actions will be taken.

Firstly, it must be noted that all this project will focus on one motor only, due to the simplicity of testing it with the prototype and the availability of replicating the same system for the other motors.

Redesign the ADCS board: the main idea of this work package is to design a configuration of new components that will achieve the desired control speed of the brushless motor. However, it must be noted that it is a hardware-in-the-loop, and it involves choosing between different hardware parts. For instance, the project will require a microcontroller, some sensors, a power control interface, and a motor actuator.

Set up the board on the CubeSat: after placing all the required components on the ADCS board, it needs to be installed inside the CubeSat. Thus, the location of the ADCS board, the brushless motor and the inertia wheel within the prototype will be determined at this stage.

Program the new control algorithm: to achieve complete attitude control of the motor PWM waves will be used. The variation of these waves will be determined by the control algorithm of the microcontroller. The algorithm should be able to collect the desire angle and provide a PWM wave signal to control the rotational speed of the motor. As for the loop, it will remind activated until the CubeSat reaches the desired angle set point.

Testing and functional verification: finally, to confirm the success of all the previous work packages, a testing process and functional verification of the prototype are required. This task will be carried out on a testing platform that utilizes compressive air to simulate the non-existent drag force that would be present in space.

On the other hand, the following activities are not included in this project.

Redesign the inertia wheel: for this project, the inertia wheel has been already determined and has been 3D printed. Therefore, there is no need to design a new inertia wheel that would be compatible with the brushless motor.

Working on the deployment moment of the CubeSat in the atmosphere: the study of the method to send the CubeSats to space and the deployment are not going to be considered. Specifically, the issue of establishing a controlled position for the CubeSat after deployment, due to the random rotation caused by deployment in space.

Consider the disturbance that the CubeSat will experience: as for this work package, disturbance in space will not be considered because they are not directly related with the aim of this project. However, any possible disturbance will be counteracted by the movement of the motors, as the microcontroller will detect a difference between the angle set point and the current angle.

Working on the movement of more than one axis: due to the additional difficulty that would arise during prototype testing if all the axes were included, this project will only focus on one axis. Moreover, if control movement is achieved in one axis, it will be replicated to the other ones.

1.3 Requirements

At the end of the project, functional prototype should meet the following requirements. It should be noted that these requirements are focused on the aim and the scope of this project, as previously discussed.

- In terms of the hardware, a brushless motor will be implemented as the previous one was not optimal. Additionally, the final project will require the replacement of the power electronic responsible for activating the brushless motor, and a new motor driver will also be needed for speed control.

  Specifically, the most appropriate alternative will be selected form each of the following components, taking into account their price.
  - Brushless motors
  - Motor driver
  - Microcontroller
- As for the software, Arduino IDE [1] will be the programming language of this project. This is because the microcontroller selected for the project is an STMicrocontroller [2], which can be configured using this free program and its libraries. Moreover, Arduino supports all functions of "C" language.
- In addition, knowledge of power electronics is necessary due to the PWM waves, which will be generated from configuration of the components and the control algorithm. The PWM waves will determinate the rotational speed of the brushless motors.
- Moreover, it will be necessary to review previous projects such as Joan Serrano's thesis [3] and Alev Yilmaz's thesis because their studies preceded this current project and contain useful information.

1.4 Justification

This thesis belongs to a broader project called PLATHON, which stands for "PLATform of integrated simulation of Hardware in the loop for Optical communications in Nanosatellites". These nanosatellites are cubes satellites measuring 10 centimeters on each side and have a mass of approximately 1,33 kilograms. All their different missions require information communication capabilities.

The Hardwar in the Loop technique is a simulation to verify the actual hardware performance in a controlled and reproducible environment, using a simulated or virtual model.

More specifically, CubeSats are design to transport information from inaccessible location on the planet to any desired database. Thus, a constellation of CubeSats in LEO orbits will provide nearly complete global coverage for communication between different CubeSats, enabling fast transmission of information to the database.

The PLATHON project is organizes by a research team at UPC ESEIAAT, tasked with a handling a variety of CubeSat function. In the case of this project, the focus is on attitude control, specifically working on a brushless motor with an inertia wheel and its motor driver.

On the other hand, the rationale for this project is based on a previous thesis done by Alev Yilmaz [4], who achieve attitude control with a MAXON motor and motor driver. Her goal was to develop a form to control the attitude of the CubeSat without worrying about the budget needed to implement more than one prototype, each of which would require four attitude systems.

Furthermore, switching to a brushless motor will improve the stability of the flywheel rotation leading to more accurate movement of the CubeSat. This will result in reduced energy consumption and faster operations.

For those reasons, it is necessary to redesign the current functional attitude board, replace the power electronic, modify the control algorithms and use a new motor driver. By doing so, a brushless motor can be implemented and a reduction of the attitude control cost of the CubeSat will be achieved.

Finally, another thesis to take into account is Joan Serrano's, which provides valuable information on the attitude controller design as cascade control loop, as well as the entire transfer function that will be used in this project. [3]

1.5 Planification

Table 1.1 Identification of work packages, their duration and precedence. (Source: own)

Id	Work packages	Duration (weeks)	Precedence
A	Start	--	--
B	Research and select the appropriate microcontroller and components to achieve the desired motor speed control.	3	A
C	Download and test sample Arduino programs to make sure the system is working properly.	4	A
D	Investigate and determine the waveforms needed to supply them to the motor.	2	B, C
E	Write and test the code for the microcontroller to implement the required waveforms.	2	D
F	Evaluate the performance of the assembly and make the necessary modifications.	2	E
G	Develop a prototype PCB to achieve a closed loop of voltage.	2	F
H	Determine the optimum location of the PCB in the assembly.	1	G
I	Design the electrical schematics and the layout of the components that will be inside the PCB.	2	G
J	Manufacture the PCB and make the wiring and connections between components, ensuring proper signal.	1	H, I
K	Perform electrical and software tests to verify connections and closed-loop board functionality.	1	J
L	Adjust the sensor signals by varying their placement and also by software.	2	K
M	Make any necessary adjustments or modifications to the system based on the test results.	2	K
N	End	--	L, M

Id	Work packages	Week 4 20/02/2023	Week 5 27/02/2023	Week 6 06/03/2023	Week 7 13/03/2023	Week 8 20/03/2023	Week 9 27/03/2023	Week 03/04/2023	Week 10/04/2023	Week 17/04/2023	Week 24/04/2023	Week 01/05/2023	Week 08/05/2023	Week 15/05/2023	Week 22/05/2023	Week 29/05/2023	Week 05/06/2023	Week 12/06/2023	Week 19/06/2023
Research and open loop operation																			
A	Start																		
B	Research and select the appropriate components to achieve the desired motor speed control.																		
C	Download and test sample Arduino programs to make sure the system is working properly.																		
D	Investigate and determine the waveforms needed to supply them to the motor.																		
E	Write and test the code for the microcontroller to implement the required waveforms.																		
F	Evaluate the performance of the assembly and make the necessary modifications.																		
Voltage closed loop operation																			
G	Develop a prototype PCB to achieve a closed loop of voltage.																		
H	Determine the optimum location of the PCB in the assembly.																		
I	Design the electrical schematics and the layout of the components that will be inside the PCB.																		
J	Manufacture the PCB and make the wiring and connections, ensuring proper signal.																		
K	Perform electrical and software tests to verify connections and closed-loop board functionality.																		
L	Adjust the sensor signals by varying their placement and also by software.																		
Functional verification and variations																			
M	Make any necessary adjustments or modifications to the system based on the test results.																		
N	End																		

Figure 1.1 Gant chart of thesis planning. (Source: Own)

2 State of the art

2.1 Introduction

Since the last century, the human goal of learning as much as possible about the world and trying to improve communication possibilities has been increasing every year. To address this issue, one of the solutions is space-based research as a way to improve, and in particular nanosatellites are optimal for a large number of missions.

The concept of CubeSat converges on the idea of a type of cubic nanosatellites that measure 10 centimeters for each edge and weighs between 1 and 1,33 kilograms, this is known as one unit (1U). Furthermore, they are planned to be modular, allowing to accommodate the necessary components for each application and reducing the additional cost and the effort to achieve the desired new configuration.

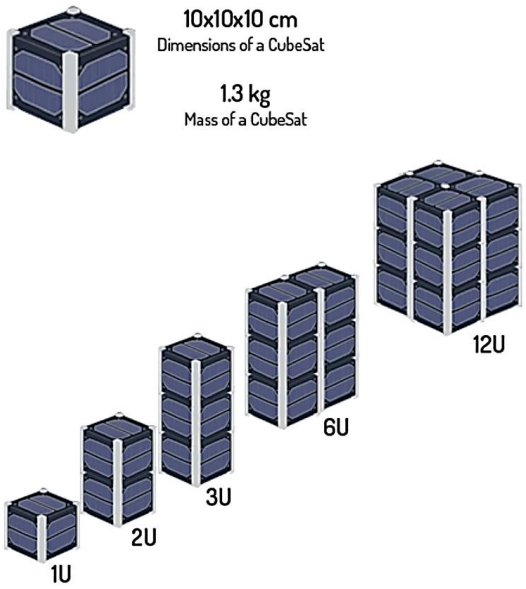

Figure 2.1 Different type of CubeSat modules. (Source: [5])

Specifically, the first CubeSat design was proposed in 1999 by Jordi Puig-Sauri (California Polytechnic State University at San Luis Obispo) and Bob Twiggs (University's Space System Development Laboratory). The goal was to allow university students to carry out the entire CubeSat process, from design, through construction, to testing and operation in space with capabilities similar to those of the first spacecraft, Sputnik-1 or Explorer-1. [6]

CubeSats have appeared in the last 15 years, and they are mainly used to test technologies that could later be implemented on larger satellites, resulting in cost reduction and less than 8 months of development. In addition, they are also used for earth observation, geolocation, signal monitoring, scientific applications, communication, and Internet of Things on a global scale.

Figure 2.2 Photo of a CubeSat. (Source:[7])

As for their lifetime, it is relatively short, so to ensure that the CubeSats will have a low-risk service they are around 2-4 years in the constellation, thus ensuring that the service is kept up to date.

In addition, there are two key facts about CubeSats related to their lifetime, during their functional period, CubeSats are usually launched into low circular or elliptical orbits, with altitudes ranging from 400 to 650 km. Such as the Low Earth Orbit constellation (LEO).

This results in an orbital velocity of approximately 8 km per second. Because of these orbital characteristics, CubeSats complete between 14 and 16 orbits per day, taking about 90 minutes for each orbit around the Earth. These orbital conditions are optimal for nanosatellites, as they offer ideal conditions for Earth observation and communication. In addition, being closer to the Earth, they are better protected from solar and cosmic radiation

On the other hand, CubeSat circular or elliptical orbits are achieved by a balance between gravitational an escape forces during launch. Due to the absence of air, there is no friction to interfere with this balance, allowing satellites to remain in orbit almost indefinitely. Once a nanosatellite reaches the end of its operational life, it enters the Earth's atmosphere and disintegrates. [5]

2.2 CubeSat subsystems

In order to be able to develop the different missions that could be assigned to the CubeSat, it must have subsystems that make it capable of handling any situation. Although the CubeSat subsystem should be the same as any other spacecraft, there is a limitation of available space. Because of this issue, subsystems must be strategically allocated within the CubeSat to ensure that all functionalities work properly. [8]

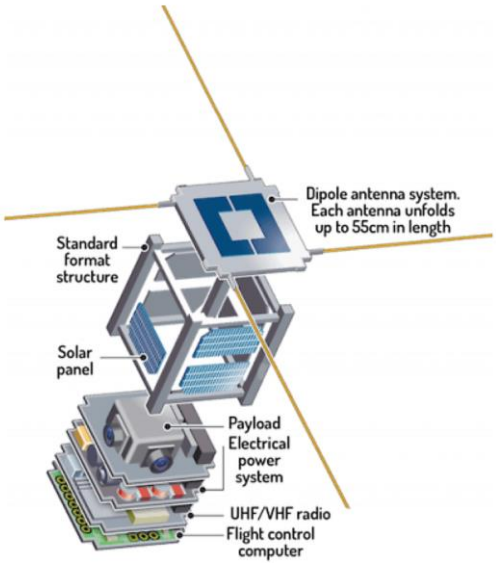

Figure 2.3 CubeSat subsystems. (Source: [5])

2.2.1 Power supply

It is responsible for distributing the power supply to the other subsystems, as well as dealing with how electrical power is obtained during the lifetime of the CubeSat.

There are several types of power sources, such as batteries, solar cells, isotropic reactors, and fuel cells. They will be determined according to their mission and lifetime, and the power supply can be provided by one or a combination of these sources. [8]

2.2.2 Telecommunication systems

It is responsible for maintaining the communication of the CubeSat between external receivers, which can be a ground station on Earth or another type of spacecraft.

The same antenna of the spacecraft is commonly used to carry out this communication, as well as the transmission and reception of information. The technology that is usually referred to this subsystem is the telemetry or telecommand. [8]

2.2.3 Data system

Data system is used to control the flow of information from sensors, instruments and antennas. In addition, this information will be sent through space and for this purpose the interaction with the telecommunication system will be implemented.

This information is stored temporarily in the computer's memory, as it takes some time for the CubeSats to reach the range of the ground station databases or to align with other satellites and communicate with each other. [8]

2.2.4 Thermal control system

In terms of optimal lifetime, throughout their flight orbits and especially during the early part of the CubeSat deployment process there are significant temperature differences that spacecraft can experience.

For this reason and considering that the hardware and the subsystems work in a certain functional temperature range, a thermal control system is necessary for their correct operation.

Specifically, there are some subsystems that needs these interactions with thermal control to increase their efficiency or works properly.

For instance, power supply system should have interactions with thermal control system, so solar panels have higher efficiency with low operating temperature. Furthermore, the performance and the lifetime of the batteries depend strongly on the temperature as they are based on chemical reactions.

Then, in some cases of the attitude control system, the temperature must be as constant as possible, such as gyroscopes. However, not all the sensors have such strict requirements, for example optical sensors works properly even though there are thermal deformations.

On the other hand, thermal subsystem is important for the spacecraft structure, because the heat of the different parts of the CubeSat will be conducted through its structure, and it will determine the flow of thermal energy. Because of this issue, the shape of the structure and the material will be chosen accordingly. [8]

2.2.5 Propulsion system

For the CubeSat to have the ability to change its orbit, the nanosatellite needs an amount of motion in the opposite direction to the desired one.

In this case, the propulsion system will be responsible for generating an impulse to change the speed of the CubeSat and, consequently, its orbit. As for the propulsion, it will be provided by a chemical engine that will be turned on for a short period of time. [8]

2.2.6 Structure

Despite the friction force that the CubeSat will experience, an optimal structure is needed to withstand high loads. The moments when this occurs are during rocket liftoff and when high acceleration is reached, creating various vibrations that the CubeSat must cope with.

The structure of the CubeSat is made up of different layers to create a sandwich structure, which provides this nanosatellite with the required stiffness and low weight. In addition, in order to achieve this goal of the CubeSat structure, the materials used are aluminum and fiber-reinforced plastics. [8]

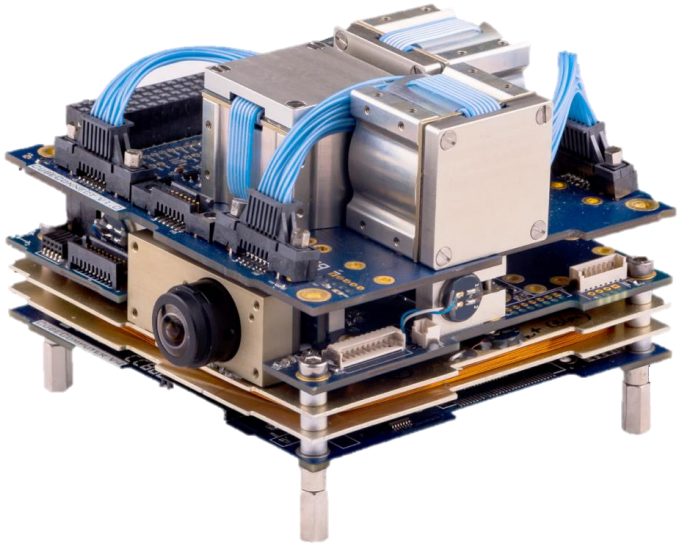

Figure 2.4 Layered structure of the CubeSat. (Source: [9])

2.2.7 Attitude Determination and Control Subsystem

The Attitude Determination and Control Subsystem is known as ADCS and is focused on measuring the current position of the CubeSat, and at the same time, calculating and performing the different changes in the actuators to reach the desired position of the nanosatellite.

This desired angle is provided by OBC, which is the brain of the CubeSat and oversees all the operations directing it and giving instructions to the other modules. Moreover, OBC is which receives and stores the data that are sent form the Earth and form the ADCS.

Then the EPS, which is responsible for producing, storing and distributing the energy. In fact, the EPS is composed by three modules:

- The photovoltaic panel
- The battery
- The power control circuit

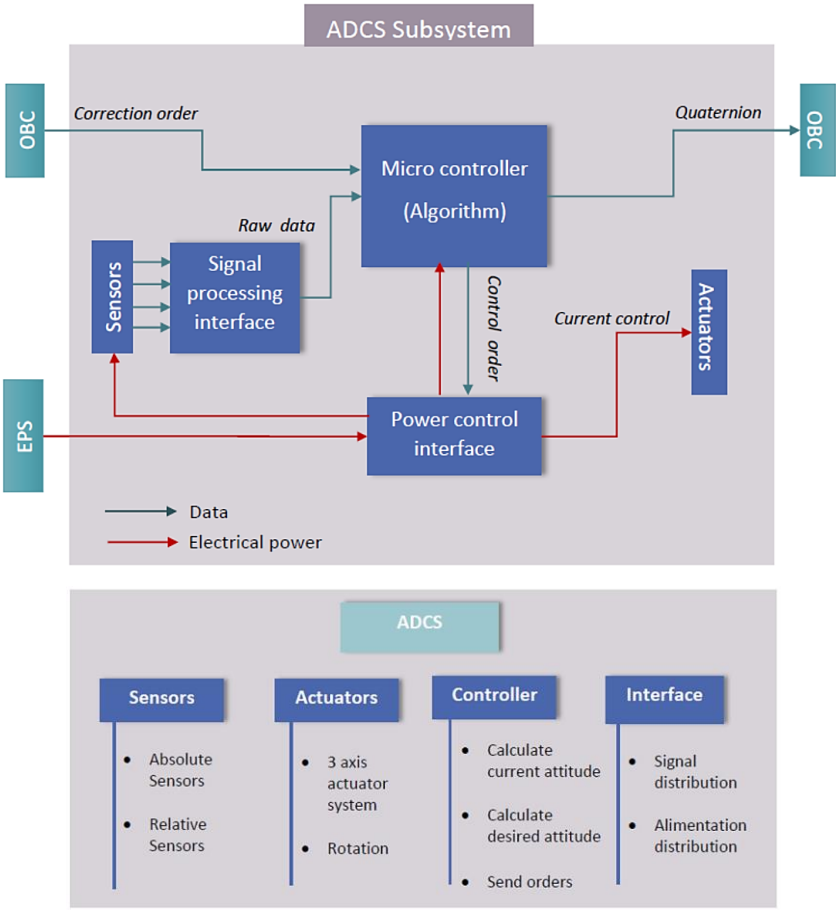

Figure 2.5 CubeSat ADCS and some characteristics of its parts. (Source: [10])

2.2.7.1 Attitude determination

As for the attitude determination, it corresponds to all the sensors that make the CubeSat capable of knowing its position in space. To perform this task there are different devices that the nanosatellite can have. Attained from literature [11] and [12].

Gyroscopes

Gyroscopes are sensors that determine changes in orientation based on the previous orientation. To achieve this goal, they contain rotating handwheels that measure the rotation of each axis. In addition, this measuring device does not have an external, absolute reference.

To function properly, gyroscopes need an initial value, and some aspects to be considered are the drift and noise that the gyroscope may experience. Regarding drift, it refers to the accuracy of the measurement, while noise is a random fluctuation of the signal, which causes some degree of error in the readings.

Currently, there are distinct types of gyroscopes available, including ring laser gyroscopes, fiber optic gyroscopes and microelectromechanical system gyroscopes. Among them there are some differences in accuracy, volume and cost.

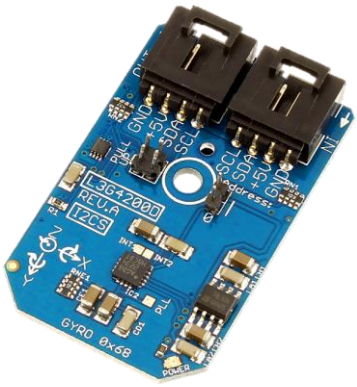

Figure 2.6 Gyroscope. (Source: [13])

Sun sensor

Solar sensors are devices that detect visible light or infrared radiation to measure the angle or angles between their mounting base and incident sunlight. These sensors have a thin input slit at the top that detects light, and as sunlight enters the device, it illuminates a sequence of photodetectors.

The digital output can be used to determine the position of the Sun. Sun sensors provide both analog and digital output signals, although the hardware design may vary. Although sun sensors can be very accurate (less than 0.01 degrees), this is not always useful in low Earth orbits, which often have eclipse periods.

Figure 2.7 Sun sensor. (Source: [14])

Magnetic sensors

Magnetometers are lightweight and reliable sensors used to detect the strength and direction of the Earth's magnetic field. In addition, the accuracy of these sensors depends on the proximity of the CubeSat's orbit to the Earth, since the Earth's magnetic field is greater the closer it is to the Earth.

They help determine the orientation of the spacecraft with respect to the Earth's magnetic field. Using three magnetometers placed orthogonally on the three axes, measurements can be taken of the three components of the magnetic field in the spacecraft body frame, allowing attitude determination by comparing the measured field with an inertial magnetic model in the on-board processor.

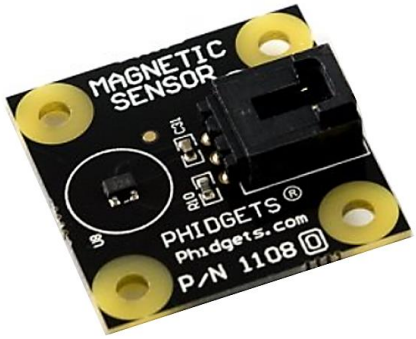

Figure 2.8 Magnetic sensor. (Source: [15])

Star sensors / trackers

Star sensors are high-precision sensors used to determine attitude. They work by detecting light from a star incident on a photosensitive surface. Charge-coupled devices (CCDs) are used to determine the location of the star on the surface. Using a star catalog and internal processing, the attitude can be calculated in three axes. These sensors can determine the attitude with remarkable accuracy within seconds of being activated.

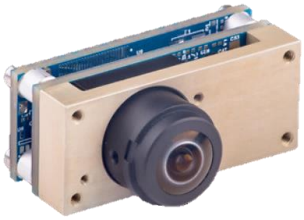

Figure 2.9 Star sensor. (Source: [16])

Earth sensors

Earth sensors use infrared technology to measure the temperature difference between deep space and the Earth's atmosphere. These sensors, which use fixed head and narrow field of view pippers that can only provide roll and pitch information.

They work by detecting infrared radiation within a specific range. The sensor mirror or prism focuses a narrow beam of light onto a sensor element, which rotates as the spacecraft turns. This motion creates a cone-shaped sweeping field of view, and the sensor electronics detect when the infrared signal from Earth is first received or lost during each sweep. The time elapsed between the arrival and loss of the signal then determines the width of the Earth, and the position of the CubeSat can be calculated.

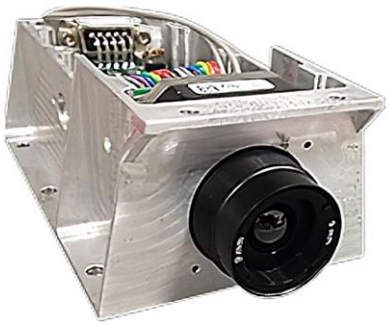

Figure 2.10 Earth sensor. (Source: [17])

2.2.7.2 Attitude control

In general, spacecraft typically use a combination of actuation systems to achieve desired maneuvers and maintain stable attitude control. For example, the following are some of the attitude control systems used by spacecraft. Attained from literature [11] and [12].

Magnetorquers

Magnetorquers are magnetic coils used as actuators on spacecraft to produce magnetic dipole moments that interact with the planet's magnetic field, generating an external torque on the spacecraft.

Their strength can be controlled by varying the current, and three orthogonal magnetorquers can generate a magnetic dipole in any direction and magnitude within their range. Therefore, they can adjust residual magnetic fields or attitude drift and desaturate momentum exchange systems but require longer operating times due to their small torque.

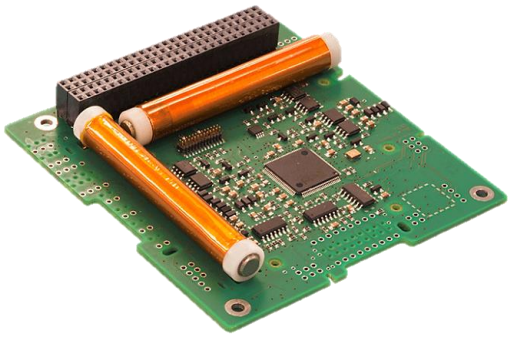

Figure 2.11 Magnetorquers implemented on a PCB. (Source: [18])

Reaction wheels

Reaction wheels, also called flywheels, are devices used to provide attitude control and stability in spacecraft by generating torque through the acceleration of a flying rotor connected to a torque motor. The reaction generated by the rotor occurs in the opposite direction of spacecraft rotation, allowing rapid rotation to the desired location.

By adding or removing power to the flywheel, torque is applied to a single axis of the spacecraft, causing it to rotate. In addition, by maintaining the rotation of the flywheel, a single axis of the spacecraft can be stabilized, and in the case of using multiple reaction wheels can provide full attitude control and stability in three axes. Besides, from this process, an attitude change can be generated to resist external forces.

The reaction wheels cannot spin indefinitely, which can cause problems if they slow down, as the spacecraft will spin in the opposite direction. Therefore, a combination of different attitude controllers will be necessary.

Figure 2.12 Different examples of reaction wheels. (Source: [19])

Thrusters

Thrusters, also known as rocket engines, are commonly used on spacecraft for orbital maneuvering and attitude control. These engines eject a material at high velocity called propellant, which generates force and torque to alter the spacecraft's orbit.

The torque produced by thrusters is limited by the size of the spacecraft and the position of the thrusters relative to the vehicle's center of mass. Although thrusters can provide instantaneous, long-range maneuvers at any time in orbit, they have a limited amount of stored gas.

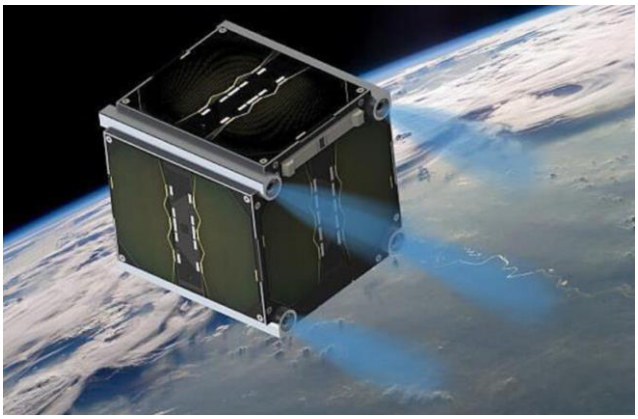

Figure 2.13 Thrusters on a CubeSat. (Source: [20])

3 Theory of electronical signal

The purpose of this section is to explain some of the theoretical techniques that this thesis will attempt to implement to operate a brushless motor.

3.1 Brushless motor operation

First of all, we must distinguish between two different types of brushless motor, as this will change the operating waveform. There is the brushless direct current (BLDC) motor, whose optimum operating waveform is trapezoidal, and the permanent magnet synchronous machine (PMSM) whose optimum waveform is sinusoidal.

The decision on which will be best for each application will depend on the complexity of the closed loop and whether position control is require. If this is the case, the chosen motor would be a brushless PMSM motor, but it will require a closed current loop which is more complicated.

However, in the case of this thesis only the rotational speed of the motor will be controlled, since positional control is not necessary. Therefore, the motor selected for this thesis will be a brushless direct current motor.

To differentiate the type of motor it is necessary to use an oscilloscope because it is unrecognizable to the naked eye. For those cases where the motor waveform is unknown, the following method can be followed.

Figure 3.1 Experimental way to know the optimal waveform of a motor. (Source: own)

In order to operate the brushless motor BLDC, a configuration of MOSFETs is needed and in the case of this thesis, it will be done with six MOSFETs. This form of operation provides a BEMF signal, which can be used for zero-crossing detection.

Firstly, the switching states of the different MOSFETs are as follows.

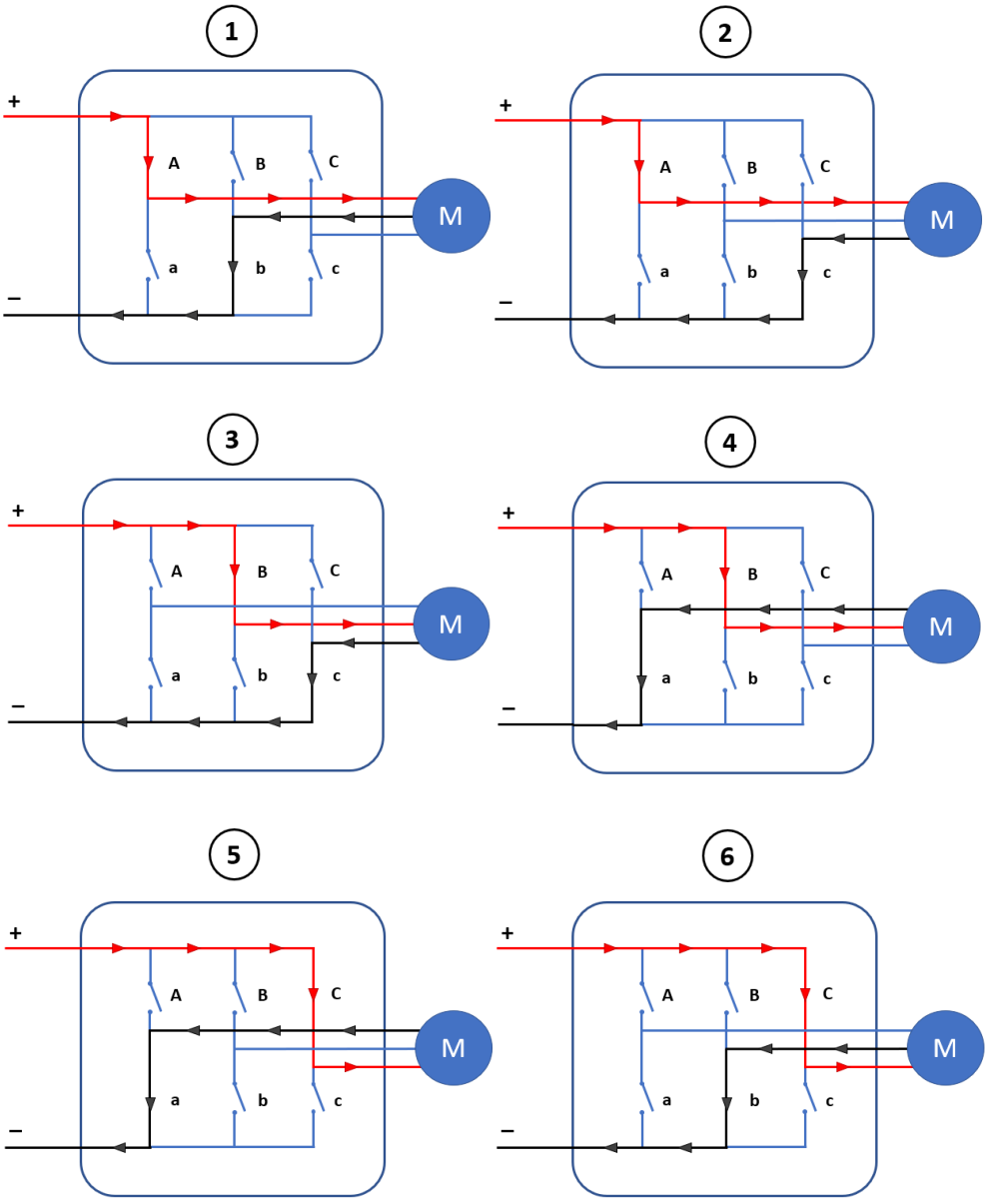

Figure 3.2 MOSFETs switching states. (Source: own)

Due to the functionality of the MOSFETs, it has been simplified with the representation of the switches and each one has been identified with a letter. Moreover, the capital letters (A, B, C) are the MOSFETs that are connected to the high voltage pole, and the lower-case letters (a, b, c) are those that are connected to the low voltage pole.

Making the representation of the different states, it is obtained the following figure that shows the signals of the three phases generated.

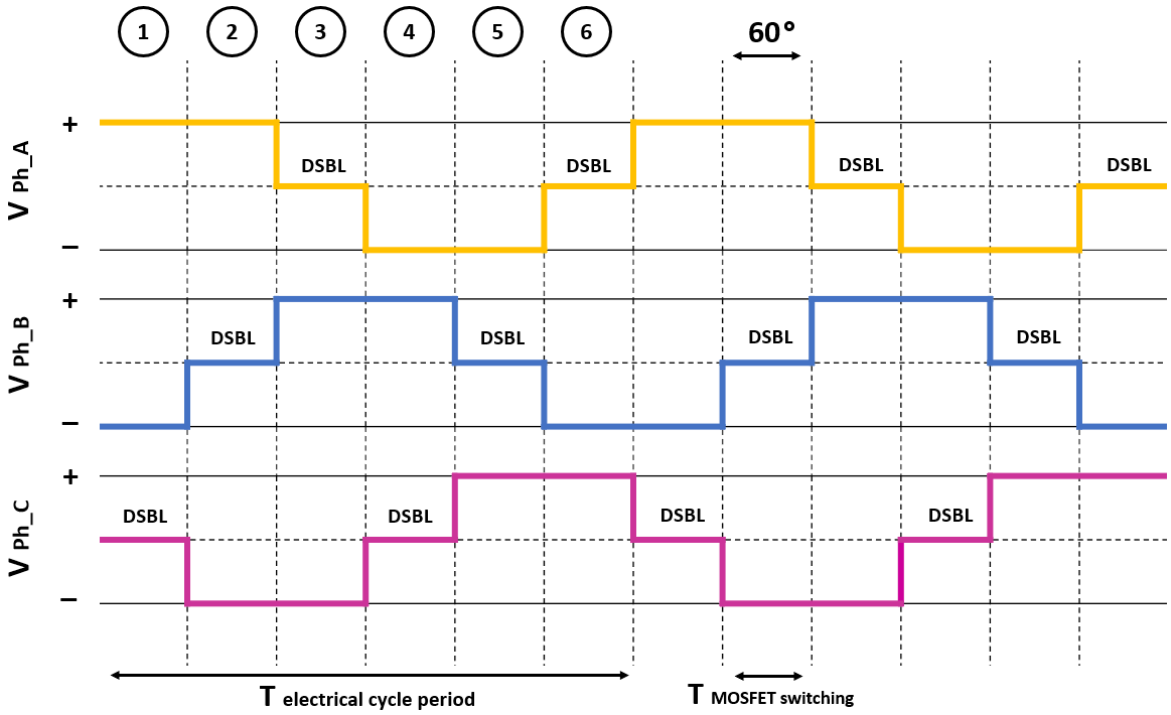

Figure 3.3 Theoretical input signals for each phase. (Source: own)

This sequence of switching states generates a square periodic signal in each phase. Analyzing one of the phase periods, each state of the MOSFETs corresponds to 60 electrical degrees, which to complete the electrical cycle period (T electrical cycle period) must pass through all six states.

Furthermore, in each electrical cycle period of each phase there are two states in which the two MOSFETs in a branch are disabled or open (DSBL). For example, in each electrical cycle period of phase A there will be two states in which the MOSFETs labeled as "A" and "a" are disabled.

On the other hand, between the different phases of the signals there is a phase shift of two states backward or forward between them, which is what generates the rotation of the magnetic field.

Also, the brushless motor BLDC used is optimal for the trapezoidal signal, so the input signal discussed above should obtain this trapezoidal shape. This can be evaluated by summing two different phase signals, as shown in the figure below.

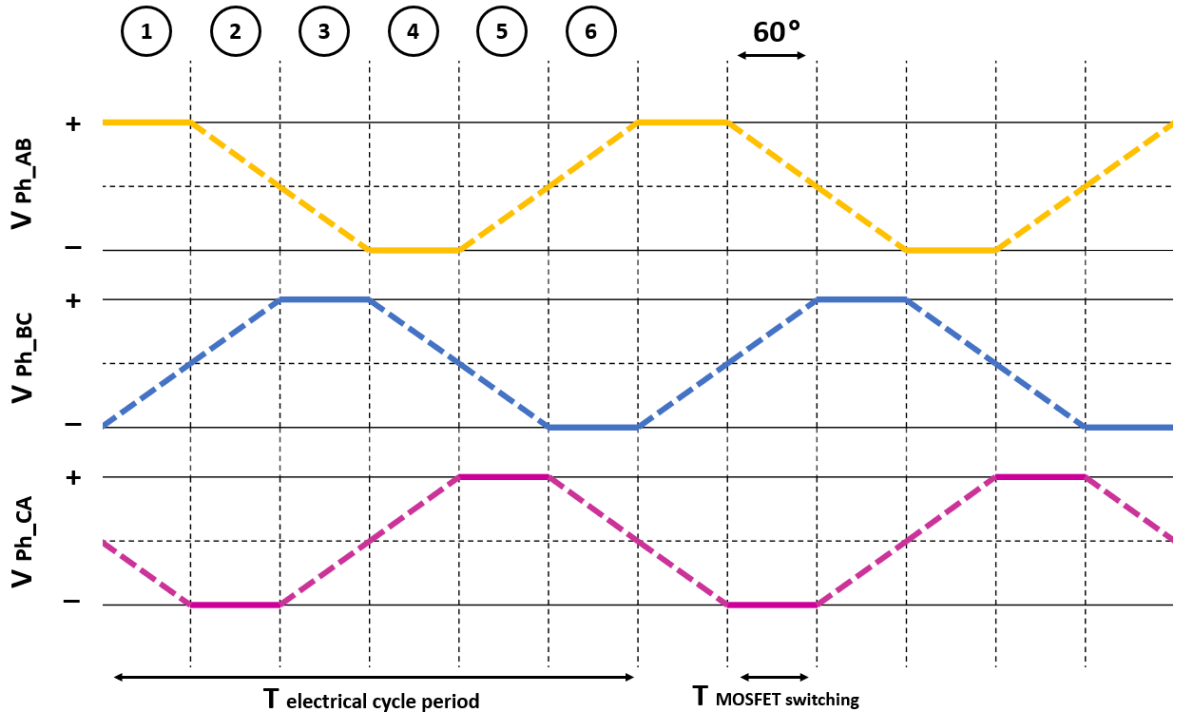

Figure 3.4 Theoretical results of combining two signals of different phases. (Source: own)

Afterwards, a signal generated by the motor operation is obtained. This signal is known as back electro-motive force and is the main way to have a sensorless zero-crossing detection. As can be observed on the following figure the zero-crossing is the point when the voltage between two phases crosses the zero volts value.

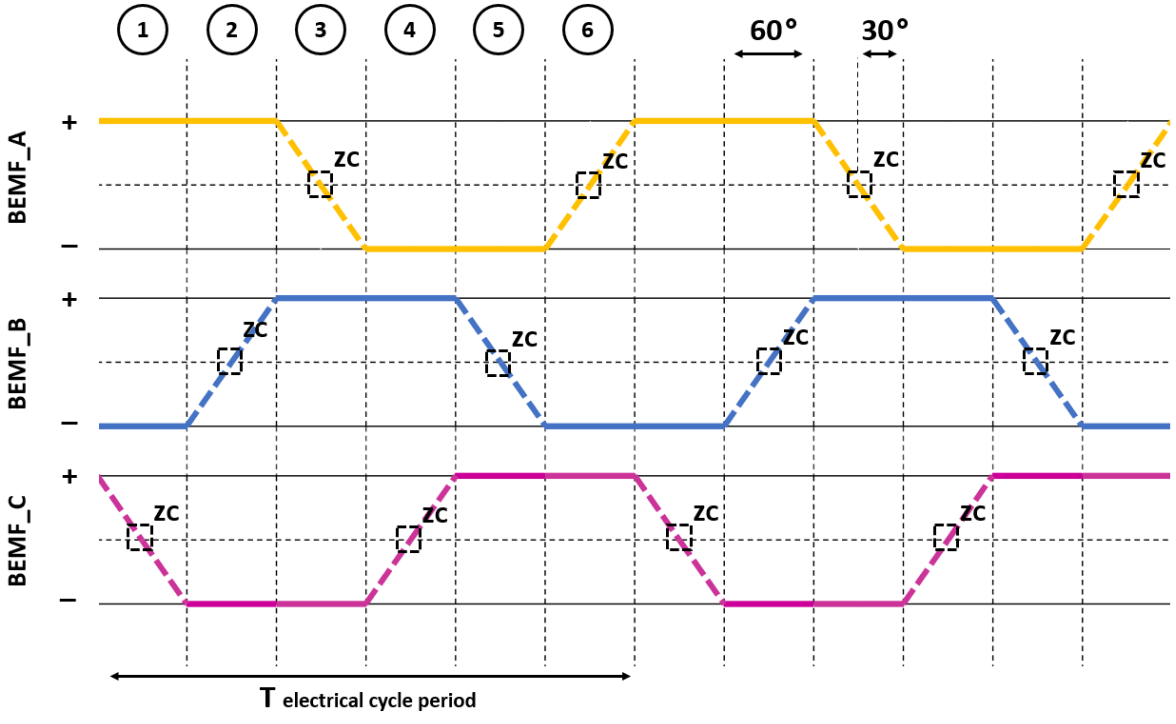

Figure 3.5 Theoretical results of BEMF signals. (Source: own)

In fact, when the voltage crosses this value, it determines the optimum commutation instant of the MOSFETs, since it is at this point that the greatest magnetic force is realized for the next movement of the motor.

All these previous theoretical arguments must be conducted by the microcontroller, and as of the code execution will control de driver. This code will be responsible for the MOSFETs switching as of the different signal waveforms.

To control this driver, it is necessary to send from the microcontroller a signal for each of the three phases, and then also three enable signals. As a result, three BEMF signals will be obtained from the motor.

The following figures will be adapted to the code and board limitations that will be used to control the driver, for this reason there are differences in the signals. For instance, negative values will not be reached, three additional signals are needed to determine the enable state, and the value of the zero crossing will change.

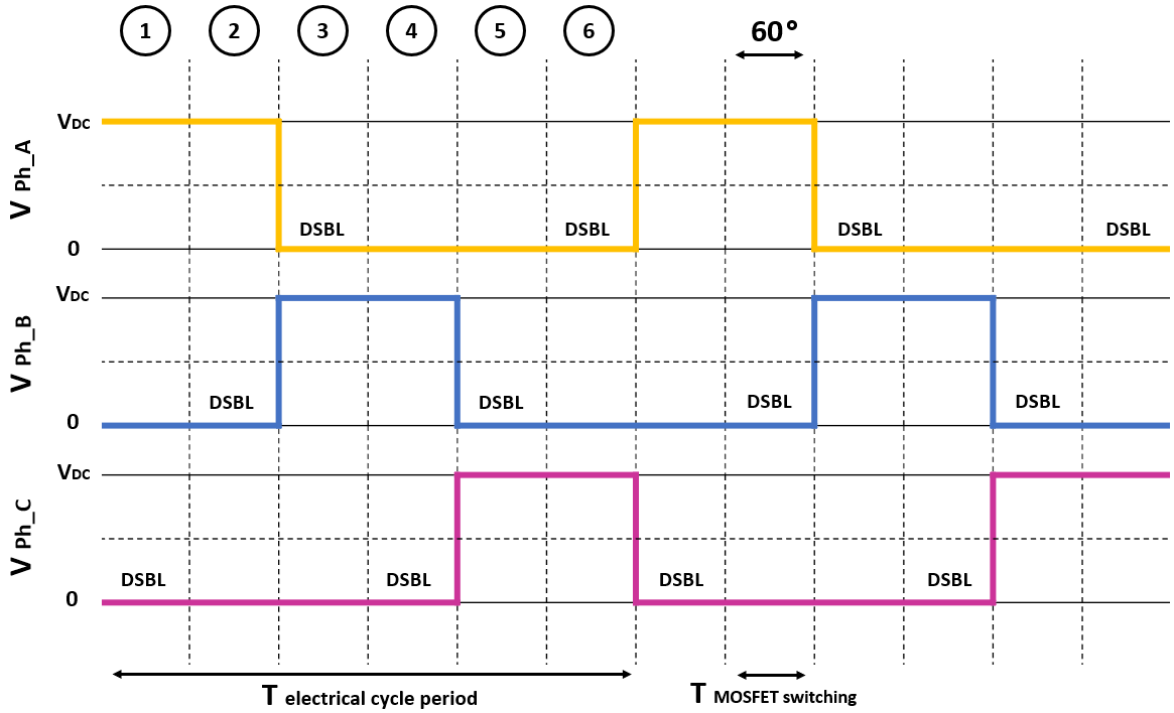

Figure 3.6 Input signals used for each phase. (Source: own)

These waveforms are slightly different because the voltage values range from high plate voltage to zero volts, values that are achieved with the PWM method at high frequency.

In addition, the intermediate states of a phase between the high voltage value and zero volts are states in which the MOSFET of that phase is disabled (DSBL), this happens due to the operation of the motor and the configuration of six MOSFETs of the driver.

Therefore, the signal waveform that the microcontroller sends to the driver in those states does not matter, because the MOSFET is disabled and will not modify the motor attitude. In the case of this thesis, on those states where the MOSFET is disabled the microcontroller will send zero volts though the phase.

Then, to send the command to the driver which MOSFET is enabled or not and when it will change its state, the code must generate a signal for each phase as is shown on the Figure 3.7.

These signals have the same phase shift between them as the previous figures, and their values will be programed on the code as high and low, which are the high voltage of the board and zero volts.

However, since these signals will determine the enable state of a MOSFET, in the figure the high value (enabled state) is represented by a one and the low value (disabled state) by a zero.

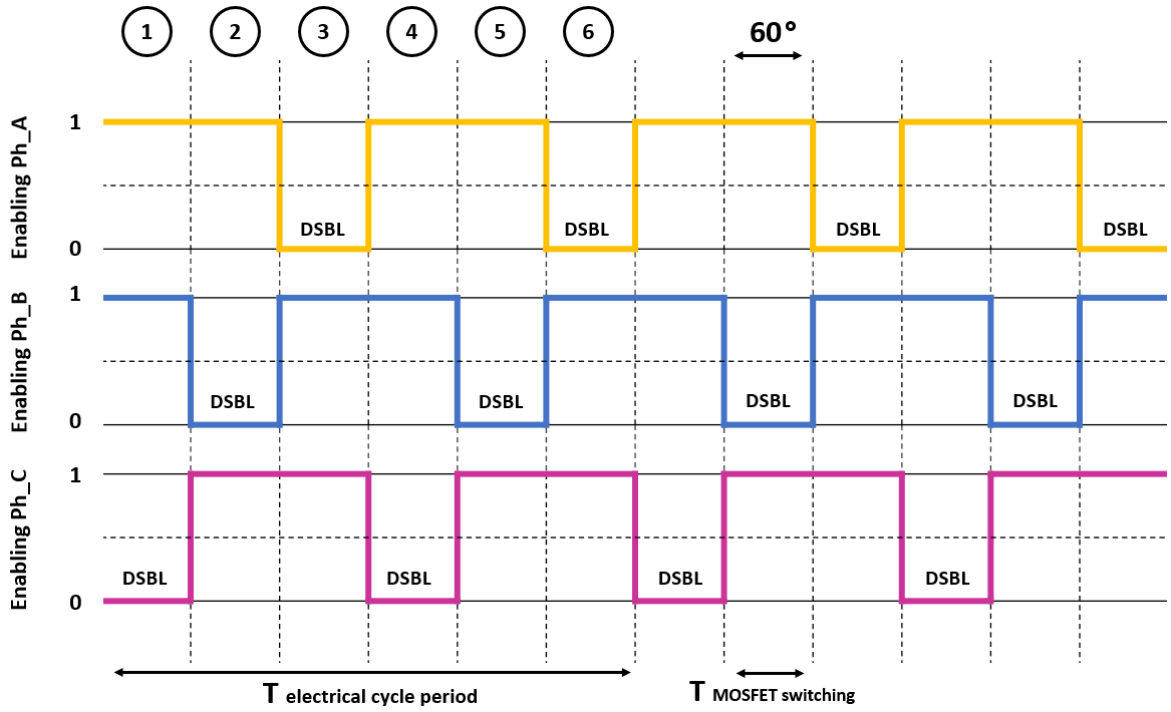

Figure 3.7 Enabling signals for each phase used in the project. (Source: own)

Afterwards, by combining of these six signal inputs we obtain a trapezoidal signal, which as mentioned, is the optimal waveform to run BLDC motor of this thesis. It is essential to ensure that the required signal form is obtained to work properly.

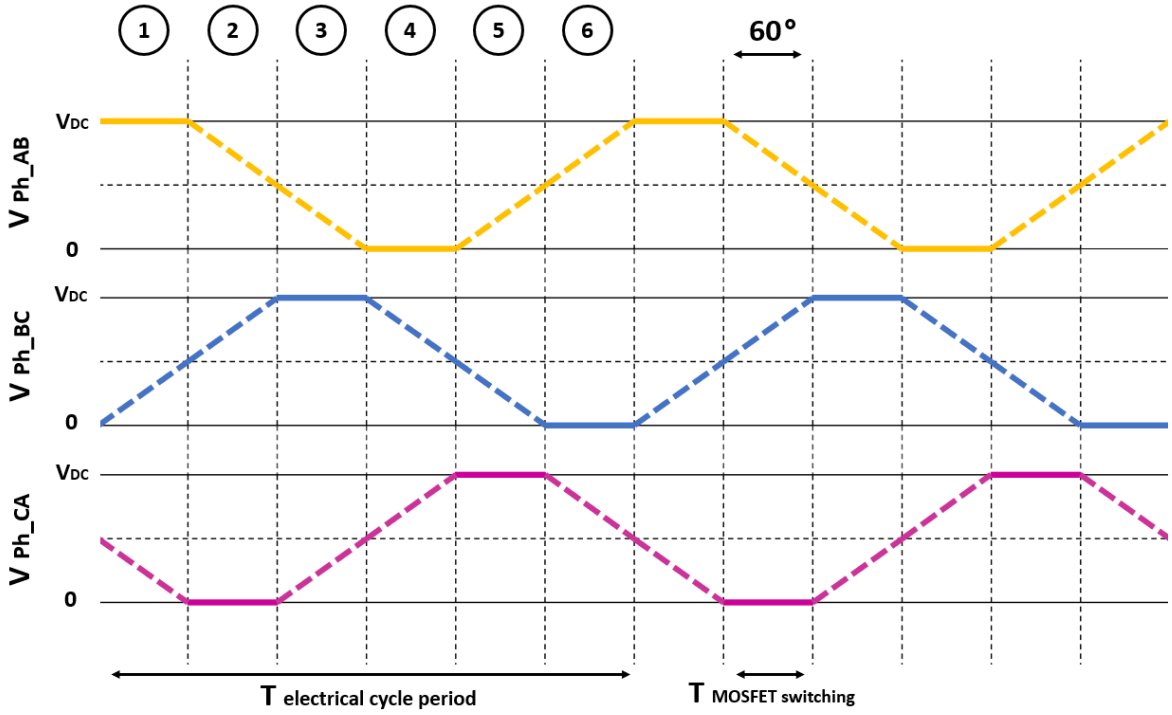

Figure 3.8 Results of the combination of two different phase signals. (Source: own)

As a result of implementing the above signals in the driver, three BEMF signals are obtained from the motor, one for each phase. These signals can be used to control the motor in sensorless mode.

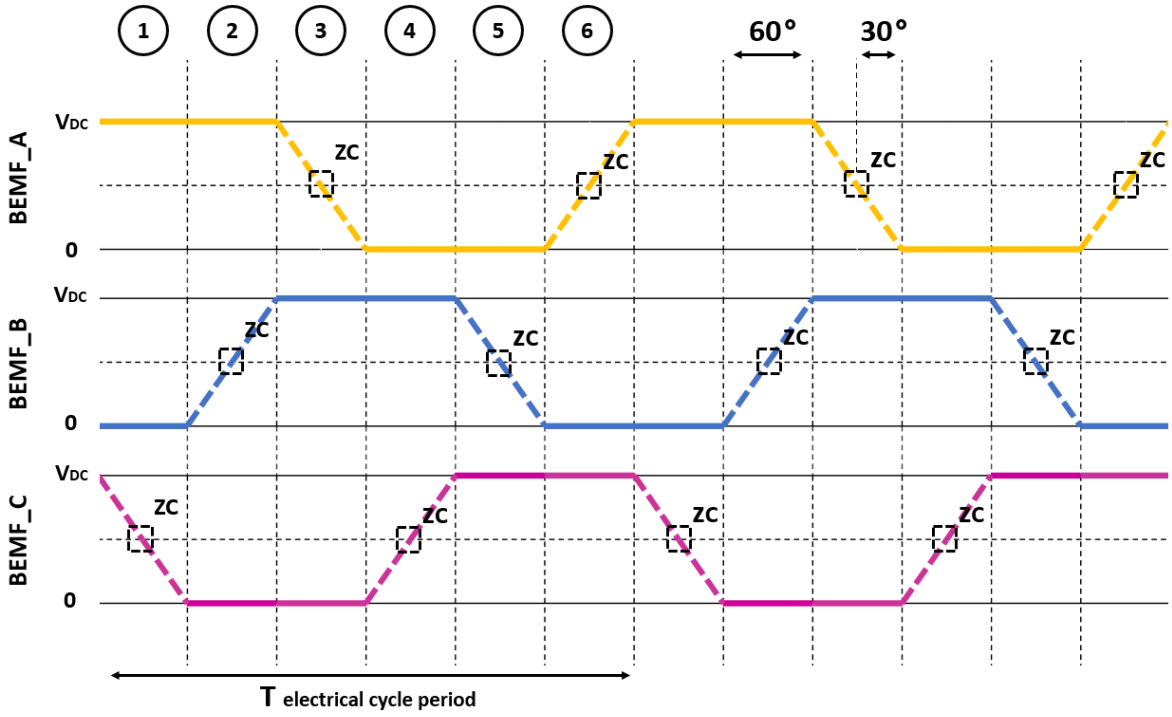

Figure 3.9 Experimental results of BEMF signals. (Source: own)

The main aspect of this figure is that the highest value will be the maximum plate voltage and the lowest voltage will be zero. Therefore, the zero crossing will not be at zero volts and will reach the value of the average voltage between the conducting phases of each state.

In case the input voltage changes its value, the zero crossing will change its position, and thus the MOSFET switching will always be at the optimum time.

Information on the use of BEMF signals and alternative methods is expanded in the voltage closed-loop control section.

3.2 Pulse-width modulation (PWM)

Afterwards, once the frequency of the commutation signals has been determined, amplitude control of these waveforms is also required to control the motor speed. As there are no brushes in the brushless motor, the voltage control must be done externally.

This is necessary because the electromotive force of all motors is directly proportional to the motor speed. Therefore, a PWM is used to control the input voltage and consequently control the rotational speed. Otherwise, with a constant input voltage the motor speed will always be constant.

This PWM signal will be sent to the BLDC motor when the MOSFET is enabled and will be inside to the signal of each phase, as follows.

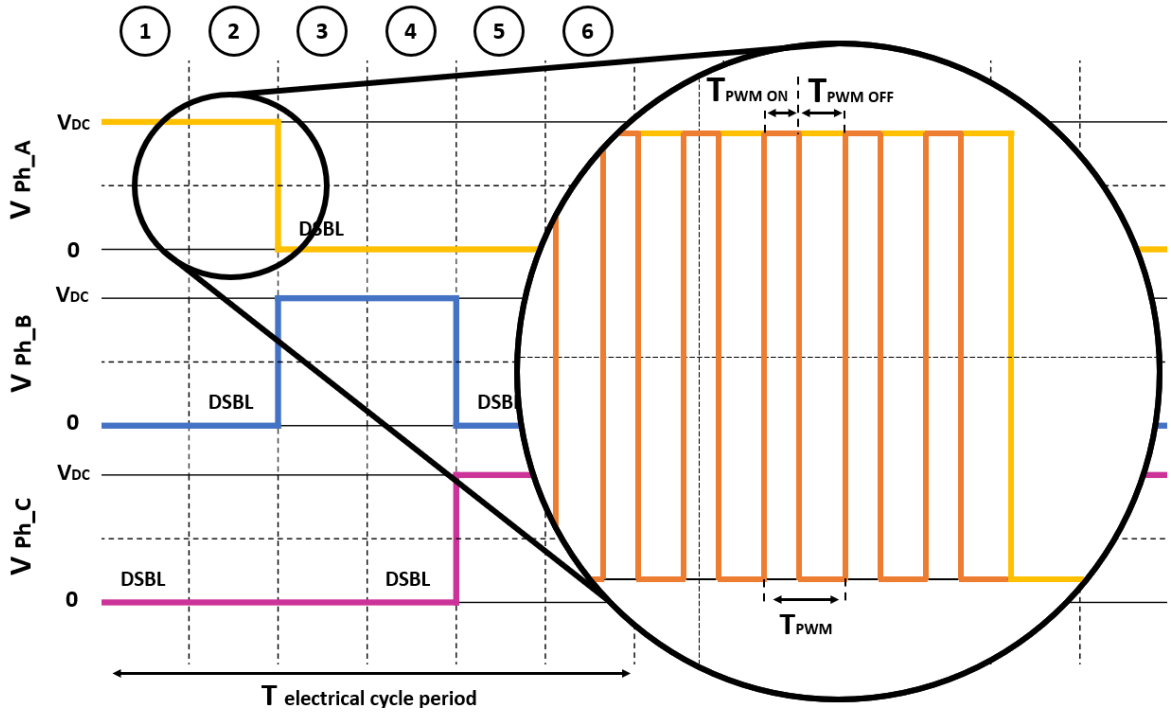

Figure 3.10 High frequency PWM signal. (Source: own)

Pulse width modulation is a method to obtain a wide voltage range with only two states of a periodic signal, high voltage (V_{DC}) and low voltage (0). This square periodic signal must be of high frequency for the motor to detect a constant DC voltage, which will be the average of the pulses.

The required frequency will be determined by the dimensions of the brushless motor and will consequently generate a ripple in the current signal. The higher the frequency, the lower the ripple in the current signal.

The period of the PWM signal (T_{PWM}) is composed of two parts, the time of the period that is at high voltage $(T_{PWM\ ON})$, and the period while the voltage value is zero $(T_{PWM\ OFF})$. Depending on the time relationship between these two periods will determine the voltage supplied to the brushless motor.

Normally, this supply voltage is determined by the percentage of the high voltage period $(T_{PWM\ ON})$ with respect to the full period of the PWM signal (T_{PWM}). Thus, the voltage sent to the motor will correspond to this percentage multiplied by the maximum voltage of the driver (V_{DC}).

For a visual representation of its operation, the following figure is provided.

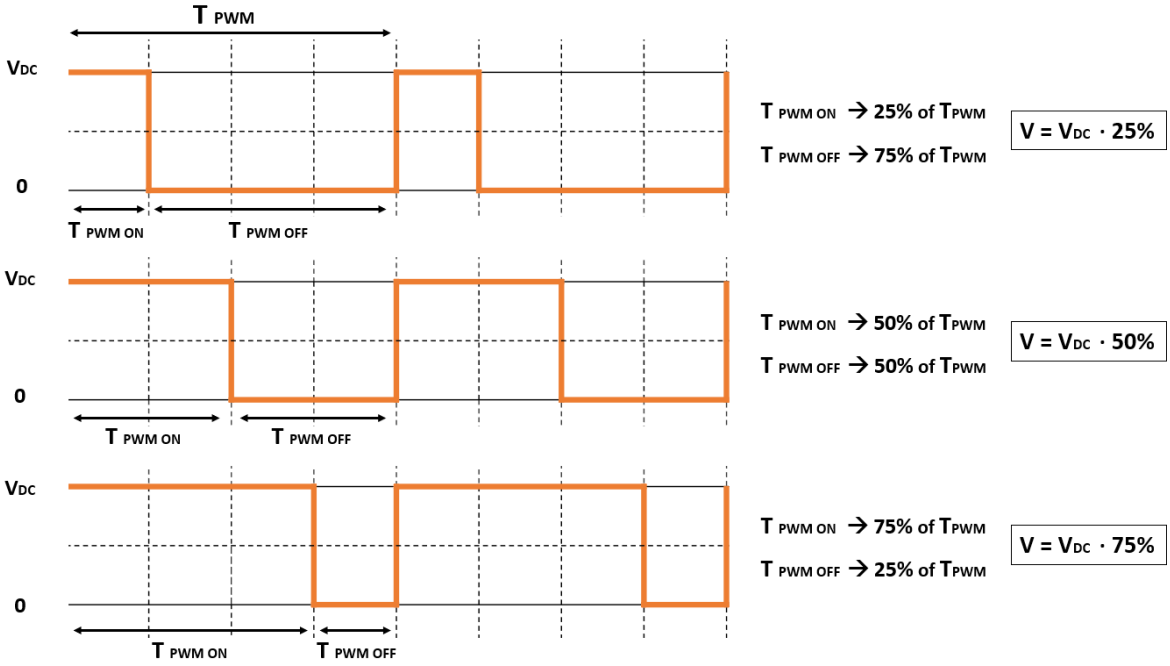

Figure 3.11 Different examples of pulse-width modulation and the value sensed by the motor. (Source: own)

Finally, both the trapezoidal signals and the PWM signal are necessary to operate the brushless motor.

In fact, these two signals work together, and a distinction can be made between the carrier signal, which is the PWM signal and has a higher frequency, and the modulating signal, which is trapezoidal in shape and has a lower frequency.

As illustrated in Figure 3.10, the modulating signal and the carrier signal are in the same package. The carrier signal is responsible for varying the amplitude of the modulating signal, while the modulating signal must have a compatible and optimal shape with the type of motor.

In addition, the modulating signal can change its frequency during motor operation by switching the enable state of the MOSFET at the optimum time. The period of this signal will determine the rotational speed of the motor and will depend on the closed loop.

On the other hand, the carrier signal is usually assigned a constant frequency during the entire motor operating time, which has been previously verified to determine the optimum frequency. This carrier signal allows the amplitude value of the modulating signal to be varied.

The last observation to make is about the antisymmetrical PWM signals, used for the operation of our motor, which means that the PWM signals will only have positive values and the minimum one will be the 0 volts.

Thus, the closed loop implementation with the BEMF method, which is explained in the following sections, generates a variation of the common point voltage value as a function of the maximum input voltage.

This idea of using antisymmetrical PWM and what it generates on the BEMF zero crossing is a required annotation for the theoretical closed-loop section, where the information will be extended.

3.3 Voltage closed loop control

As soon as we have the control of the commutation frequency and the control of the input voltage, a closed voltage loop can be made. In that way the motor will adapt the switching frequency with the rotor speed, and that speed will depend on the input voltage.

Therefore, a closed-loop voltage control will be implemented. Although, it is not the best option to have an accurate torque control, it is the simplest closed loop that can be realized to have a first contact with attitude control.

In addition, the process that the loop will follow is that increasing the input voltage will generate higher speed, since in motors these two aspects are directly proportional. This increase in speed will generate a higher frequency of detection methods, and vice versa.

During this thesis, two methods will be explained to obtain this voltage in closed loop, the method without sensors or also known as BEMF method, and the method with sensors that will be explained using Hall effect sensors.

3.3.1 BEMF method

First, it is essential to know the type of connection of the wire coils, which for this thesis the motor has a Y connection. That requires a physical connection between 3 phases, which will be called as the common point (COMM).

However, since only two phases are enabled, the common point value will be the average voltage of these two phases, and the third phase will be used to measure the BEMF. Thus, when the voltage measured on this disabled phase crosses the common value, the code will toggle the MOSFET enable setting.

To represent this information, we evaluate the first state of the period of the electrical cycle.

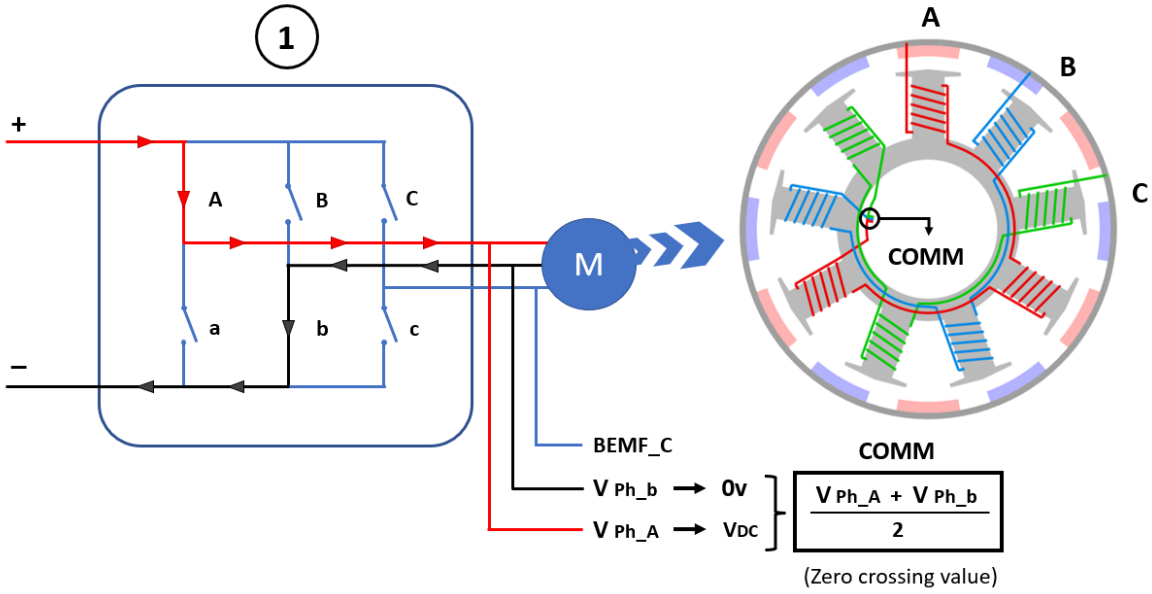

Figure 3.12 Representation of state 1 of the MOSFETs considering the signal of each motor wire. (Source: own and [21])

The BEMF signal is the sum of the input voltage supplied to the phase in each state and the return electromotive force generated in that phase and state. Therefore, if we analyze the BEMF of phase C, those states in which phase C is assigned to a high or low voltage the back electromotive force is not easily detectable.

However, in the two states in which all the C-phase branches are opened, the return electromotive force generates a current in the opposite direction to the input current of the previous state.

This situation is caused by the rotation of the fixed magnets which generates a variation of the magnetic flux density in the coil wires, and consequently, a voltage in the opposite direction is obtained. With theoretical support from Faraday's law of induction and Lenz's law.

Therefore, the slopes of BEMF signals decrease the voltage when the previous states have been on high voltage, while in case that the previous states have been on low voltage the signal increases its value.

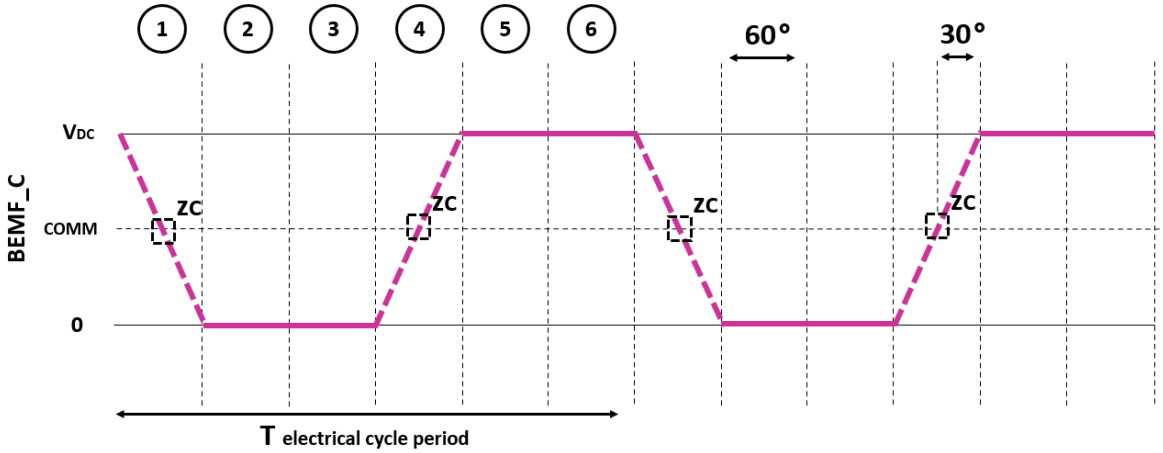

Figure 3.13 BEMF signal of the phase C. (Source: own)

This is why the BEMF signal is useful to determine a moment to switch the MOSFET configuration.

In fact, the value of the BEMF in the open states is related to the rotational speed of the motor, and the moment the BEMF signal crosses this threshold value it means that it is in the optimal position to switch the states of the MOSFETs.

The greater the slope of the BEMF signal, the faster the motor rotates. And, consequently, the period of the modulating signal is reduced.

Also, as mentioned in the previous section, an antisymmetrical PWM signal will be used to drive our motor. And this means that the common point voltage will vary by varying the value of the high voltage, which depends on the input PWM signal. This situation will generate a variation in the period of the modulating signal.

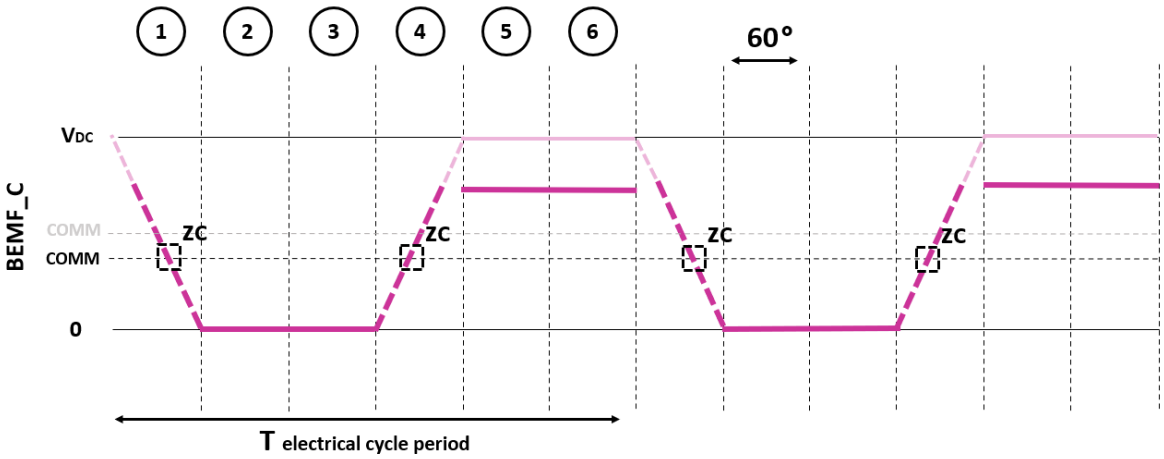

Figure 3.14 BEMF signal of phase C with lower input voltage. (Source: own)

Apart from that, almost never the common point is available by default and especially in cases where the brushless motor has small dimensions. Therefore, it can be done externally as follows.

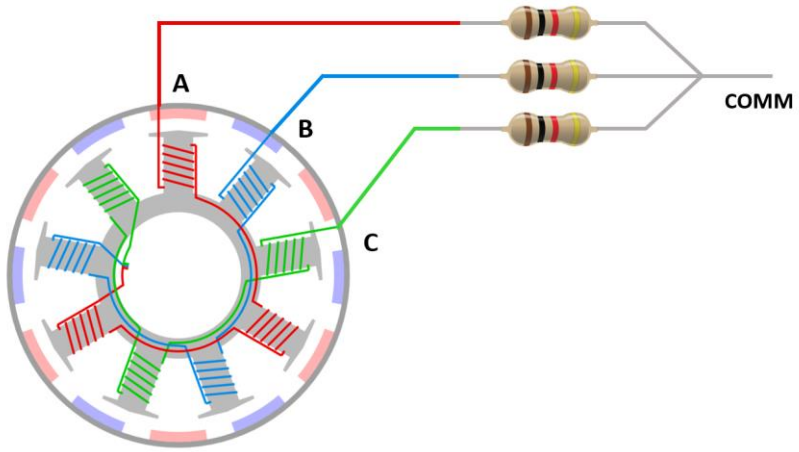

Figure 3.15 Experimental way to measure the common point between the phases. (Source: own and [21])

Where three resistors are required one for each phase and then the other pole of those three resistors connected. The magnitude of the resistors is not from a real example.

A limitation of this method is that the motor must have a minimum speed for the BEMF to determine the switching moment, otherwise the signal is too weak.

Some practical processes for this method have been developed from STMicroelectronics, this document will be available on the annex of this thesis. [22]

3.3.2 Hall effect sensors method

On the other hand, the detection method can be performed from Hall effect sensors, where usually three of them are the number of sensors used. However, it is possible to have a smaller number of sensors but, in that case, more computational resources will be required.

The placement of the Hall effect sensors is essential to obtain an accurate signal, which will be used to determine the switching moment of the MOSFETs. This placement will be 120 electrical degrees as the phase shift of the three signal phases between them, thereby sensing all three phases.

In addition, although there are a multitude of Hall effect sensors, in this thesis a SOT-23 unipolar Hall effect sensor will be implemented. It will turn on, or also known as the saturated state, when there is a south pole near the sensor, and it will conduct the input voltage to ground. In the other case, when there is a north pole near the sensor, the sensor is turned off and the input voltage is passed to the output signal.

As can be seen in the following figure, it will result in a digital signal where the values will be a high voltage or 0v.

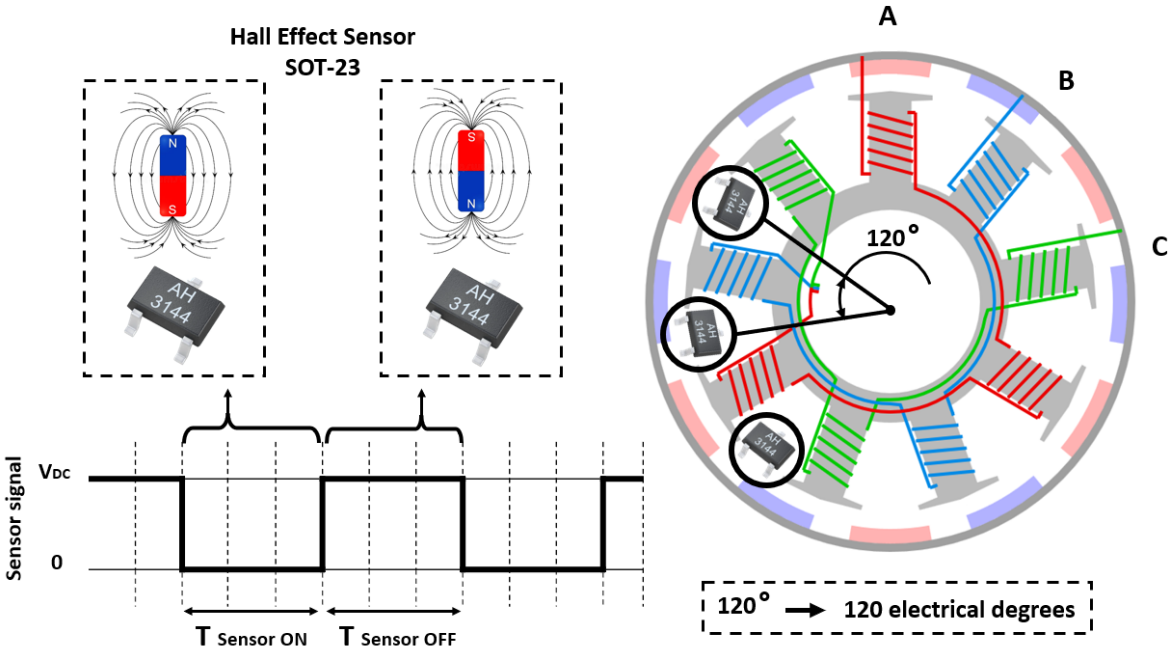

Figure 3.16 Representation of the sensor positions and its signal. (Source: own and [21])

Like the BEMF method, this signal is related to the rotational speed of the motor and the moment the signal changes value is the optimum position to switch the state of the MOSFET. Each sensor will determine the switching time of one phase, which means that each signal will have two variations of its value per electrical cycle period.

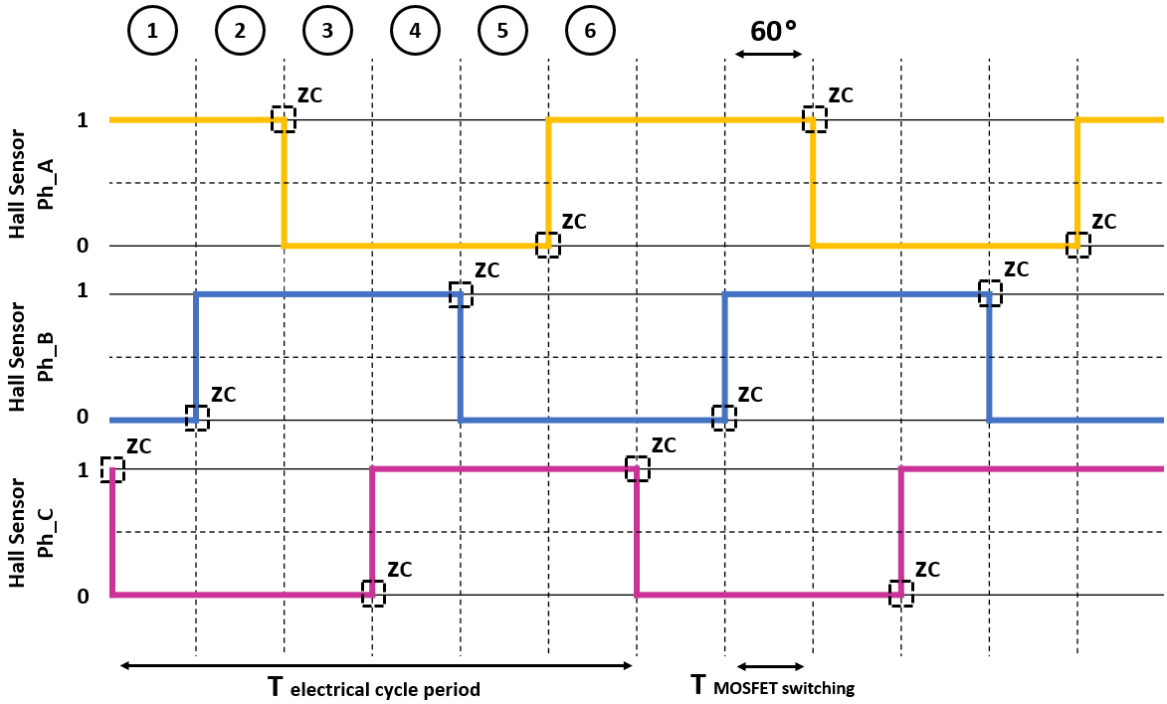

Figure 3.17 Theoretical sensor signals for each phase. (Source: own)

The sensor signal will change its value depending on a certain value of magnetic flux density, this value is specified by the manufacturer.

Finally, in this method, it is not mandatory for the motor to have a minimum speed, since the sensor always detects the current position of the rotor.

Then the period of these signals will vary as a function of the motor speed and will have a payback in the period of the modulating signal that the code sends to the motor. Therefore, we have a closed loop to ensure that the signals supplied to the motor are the most appropriate at any given time.

4 Instrumentation

The purpose of this section is to mention the thesis instruments and provide links to more technical specifications.

4.1 Devices and physical elements

First, the control device will be a microcontroller model STM32 Nucleo-F411RE, which is responsible for executing the code and generating the signals. The developer of this board is STMicroelectronics. More information at [23].

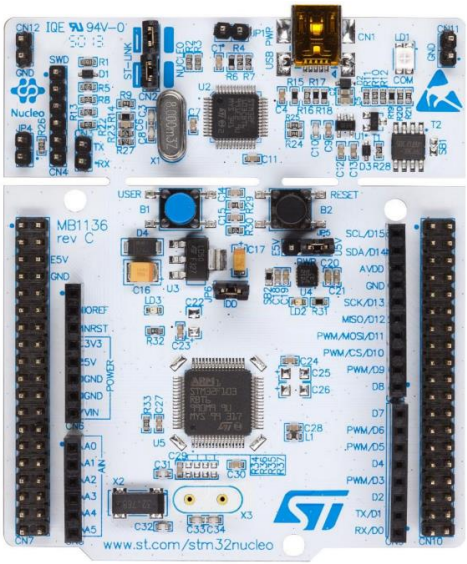

Figure 4.1 Microcontroller STM32 Nucleo-F411RE. (Source: [23])

Then, X-Nucleo-IHM07M1 driver from STMicroelectronics. This device receives the commands from the microcontroller and applies them to the motor with higher voltage range, it also has the MOSFET configuration that generates the waves. More information at [24].

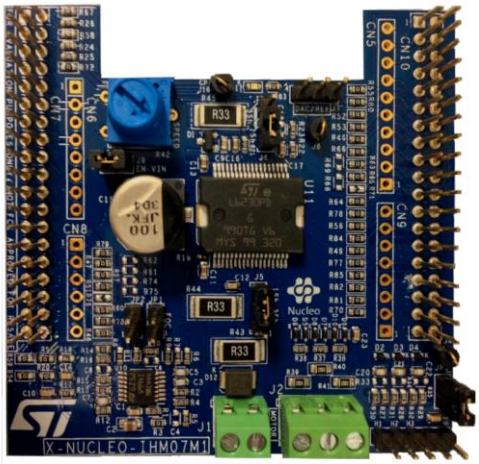

Figure 4.2 Driver X-Nucleo-IHM07M1. (Source: [24])

And the brushless motor that must be controlled is the model EMAX 1104 4300K. More information at [25].

Figure 4.3 Brushless motor EMAX 1104 4300K. (Source: [25])

Furthermore, to achieve higher inertia with the rotation of the brushless motor, a flywheel will be implemented on the rotor. This flywheel is a prototype and is manufactured with the UPC 3D printer. [26]

Figure 4.4 Flywheel manufactured by UPC Terrassa 3D printer. (Source: own)

Also, to conduct all the testing process is required tension funnels to supply tension to the circuits. Model FA-665B doble 2x30V,5A laboratory funnel (auxiliar 5V,3A).

Figure 4.5 Tension funnel. (Source:[27])

In addition, two oscilloscopes will be used to evaluate the generated signals. One is a digital oscilloscope manufactured by Tektronix, while the other is a mixed-signal oscilloscope manufactured by Agilent.

They are also very useful to find out any problems that may be present

Figure 4.6 Tektronix TDS2024B digital oscilloscope and Agilent 54621D mixed-signal oscilloscope, respectively. (Source: [28] and [29])

Finally, a soldering iron, tin wire and a stand with a magnifying glass will be used to make solid connections and prototype plates. In cases where a temporary connection is required, wires with adapters will be used.

Figure 4.7 Connection tools. (Source:[30])

4.2 Programs

As for the programs used to develop the experimental part of this thesis, the following two programs were used.

One of them has been used to program the code and send it to the microcontroller, this program is Arduino IDE a free software that allows you to add many libraries and codes for free.

In addition, it is based on the C and C++ languages and allows the user to have a viewer and a monitor that displays the program information, as long as there is a cable connected from the computer to the board. More information at [1].

Figure 4.8 Software Arduino IDE. (Source: [1])

On the other hand, the second program used during this thesis is KiCad EDA, which is a free software package that allows the user to design electronic circuits and then make the printed circuit from the previous schematic.

Moreover, anyone can perform the whole process of creating a printed circuit board from this software, since it has two-dimensional and three-dimensional views that facilitate the final design of the printed circuit board. More information at [31].

Figure 4.9 Software KiCad EDA. (Source: [31])

Finally, due to the freedom of use of these software, communities are generated and, in these forums, you can find very good support to solve any problem you may have.

5 Project implementation

The following section will show the results obtained during the process. In addition, we will discuss the decisions made by comparing the results obtained with the previous theoretical signals and evaluating the brushless motor performance.

5.1 Experimental results and decisions taken

First of all, it is essential to know the optimum waveform of the motor to be put into operation. Therefore, as mentioned in the theoretical section, the first setup has been carried out with the motor of this thesis to verify its optimal waveform.

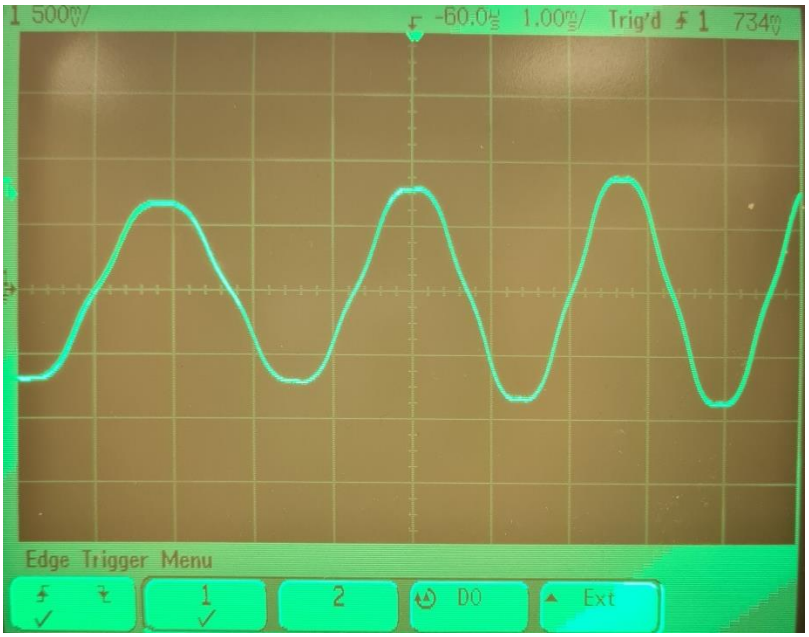

Figure 5.1 Signal obtained to determine the optimum motor waveform. (Source: own)

As can be seen in BLDC motor case, its optimal waveform is trapezoidal, and to determine this it is required to achieve a rotation of the motor. For convenience, it is better to maintain a constant rotation to obtain a constant signal on the oscilloscope.

At this point of classifying which waveform obtained, it is common that it resembles a sinusoidal shape although its optimal waveform is trapezoidal.

This situation occurs because both the trapezoidal and sinusoidal signals are actually similar to each other. But it will only be sinusoidal in the case where the signal is perfect as a sinusoidal function, otherwise it will be trapezoidal.

In fact, most of the brushless motors used are BLDC, which means that their waveform is trapezoidal.

Once is known the optimal waveform, is required sending to the motor some specific signals to obtain that waveform as a result.

Therefore, the main part of its attitude control is performed by the code and the electronic signals that the microcontroller supplies to the driver. Thus, considering the shape of the signals that are required to motor rotation, the input voltage signals for the three phases are generated as follows.

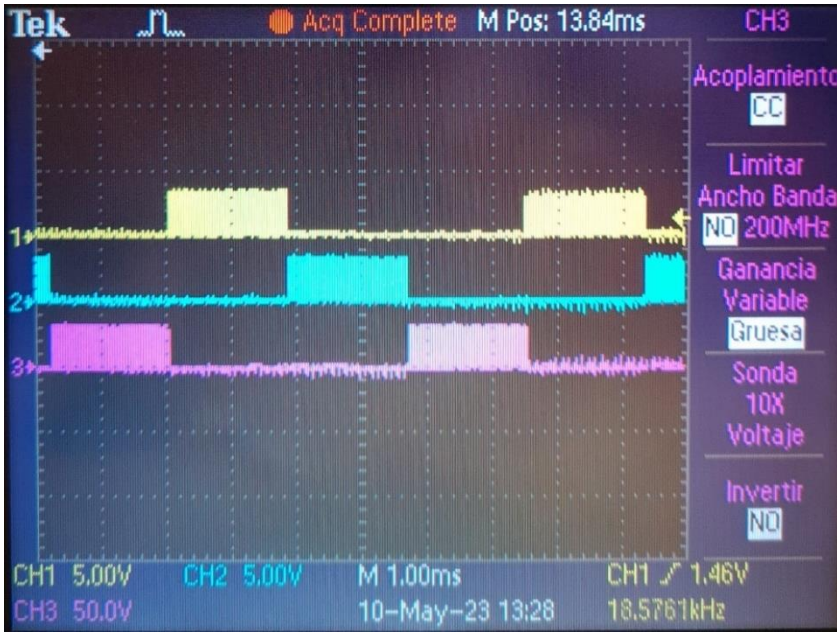

Figure 5.2 Experimental input signals used for each phase. (Source: own)

As explained in the theoretical section, those signals are the modulating signals that have a frequency around 180Hz, and each phase is activated one third of the electrical cycle period. Those signals of the Figure 5.2 are ordered as phase A, B, C from top to bottom.

On the other hand, within the modulating signals there are the carrier signals that have a higher frequency reaching the value of 80kHz, and they will be important to vary the voltage supplied to the motor from the PWM signals. The following figure shows some examples of the PWM signal, which is modified by the potentiometer of the microcontroller board.

In addition, the smaller the motor dimensions, the higher the frequency to be applied to the carrier signal, since its coils or also called inductance load are smaller.

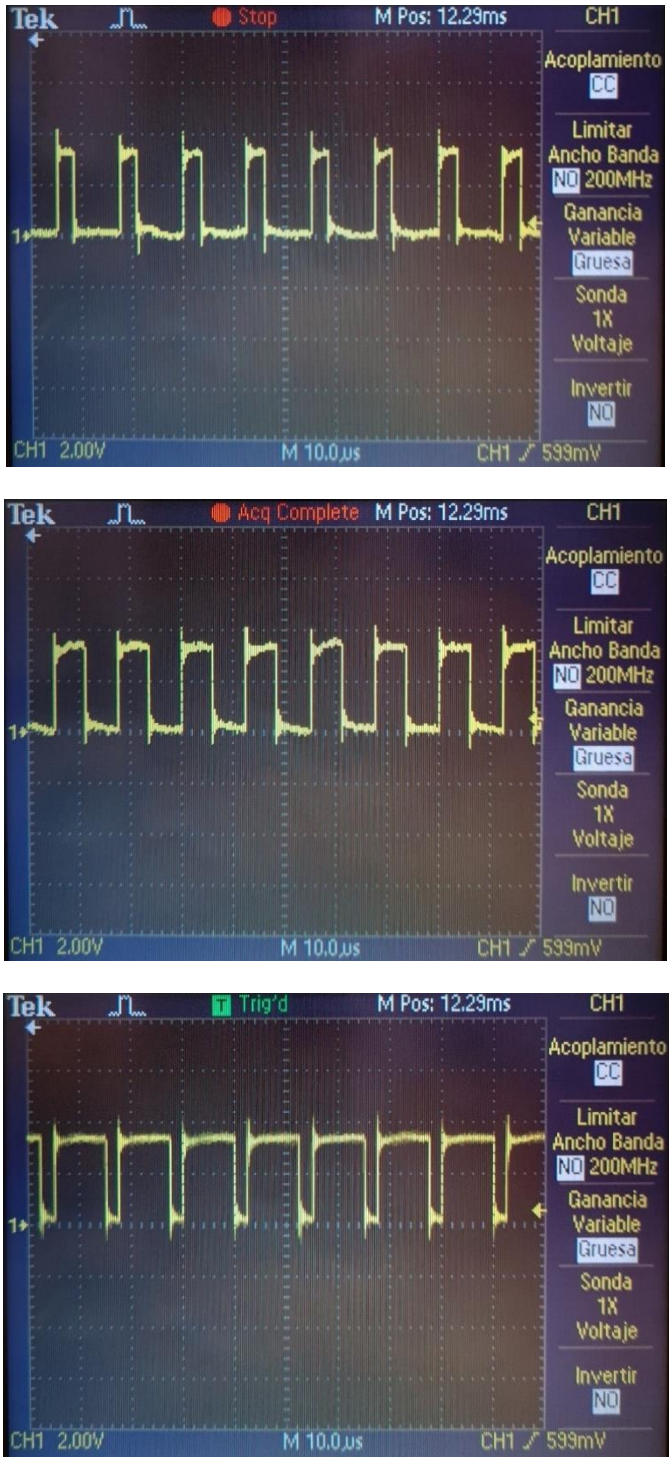

Figure 5.3 Experimental PWM signal with different width. (Source: own)

In the case of these three PWM signals they are the same carrier signal of phase A but with different pulse width. The first image in the figure is a PWM signal with 25% duty cycle, and each image below is a PWM signal with 25% duty cycle higher than the previous one.

In coordination with these previous signals, enable signals are also generated to complete an open loop. This form of operation makes the motor capable of rotating at a fixed speed, but it is not the best because the code is not generating the magnetic field at the optimum time to make the greatest force. Therefore, the current consumption will be considerably high.

After adding this part of the code, the signals that will enable and disable the MOSFETs are ready, and these three generated signals look like the following figure.

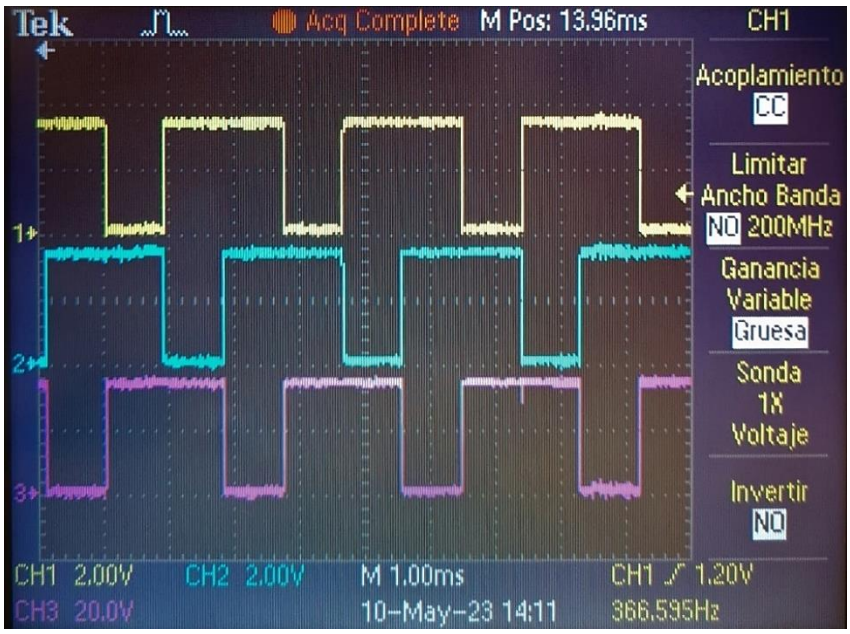

Figure 5.4 Experimental enabling signals used in the project. (Source: own)

As can be seen there are always two MOSFETs enabled, and the disabling process is in cascade. This type of signal allows using the BEMF method to make measurements on the wire of the disabled phase, as has explained on the theoretical section.

Up to this point in the thesis, the open-loop control configuration is as follows.

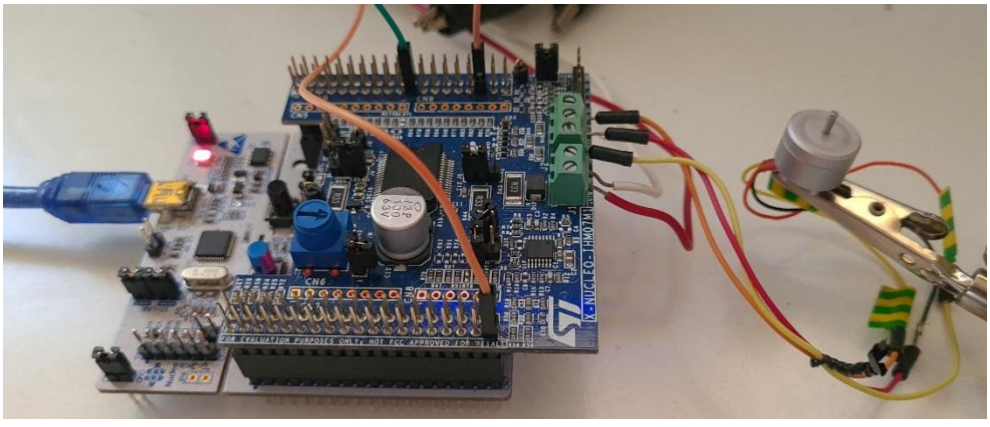

Figure 5.5 First assembly with open loop control. (Source: own)

Once the assembly of Figure 5.5 has been prepared and the motor is running, it can be evaluated if the waveform obtained after applying all the previous signals is the optimal waveform that it has been determined.

To obtain the representation of this signal it is required to do it with the motor running and connect two of the three phases to the oscilloscope. Where one of these two phases will be connected as the oscilloscope ground signal.

And as shown in the following figure, it can be observed that the waveform obtained is trapezoidal.

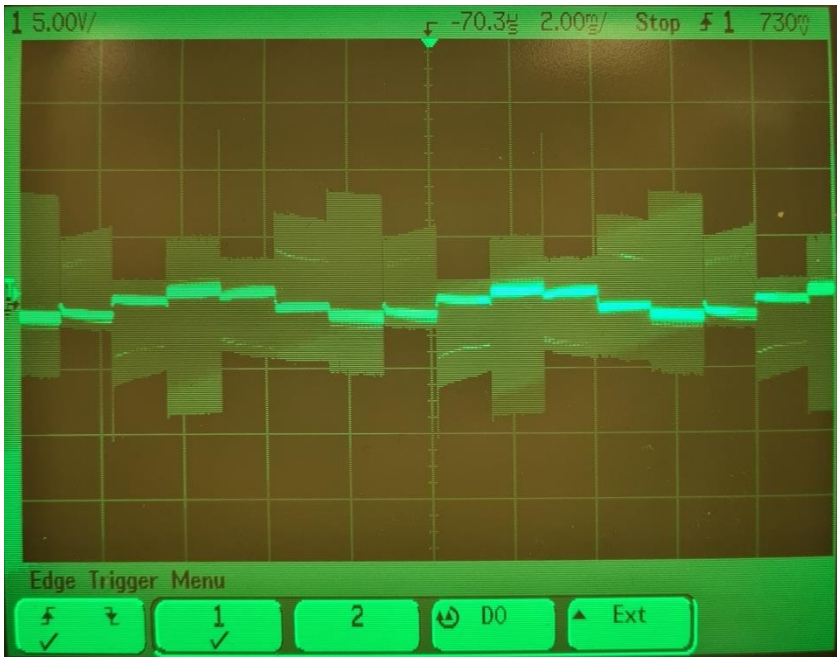

Figure 5.6 Trapezoidal signal obtained by the motor rotation. (Source: own)

This open loop control allows the motor to run at a fixed speed. In fact, this speed will be a function of the period we encode for the modulating signal and the variation of the carrier signal will be only to slightly increase the torque and its current consumption as well.

In addition, it has been observed that when we apply some resistance against the motor rotation the current consumption decreases a little, while the good behavior against this perturbation should be that the consumption should increase slightly to have more torque and avoid motor stall.

Therefore, the next step of the thesis had to be the implementation of a closed loop, and after considering the different options, the voltage closed loop has been chosen. The main reason was the availability of the requirements to implement it and that no further investment was needed, since the MOSFET configuration has the advantage of measuring BEMF.

Moreover, the company STMicroelectronics, developer of the boards being used for this thesis, has documentation that discusses the BEMF methodology and some alternatives to control it. This documentation is included in the bibliography of this thesis [22].

Once implemented in the code, we could now measure the BEMF signals of each phase.

However, due to the low BEMF voltage and the low inductance of this BLDC motor, the BEMF signal has a lot of background noise. The reason for this coupling is that the noise voltage is considerable compared to the voltage of the BEMF signals. In addition, the high frequency of the carrier signal adds some noise.

This makes difficult to recognize the theoretical shape of the signal, as mentioned in the previous section.

The following figure shows the BEMF signals.

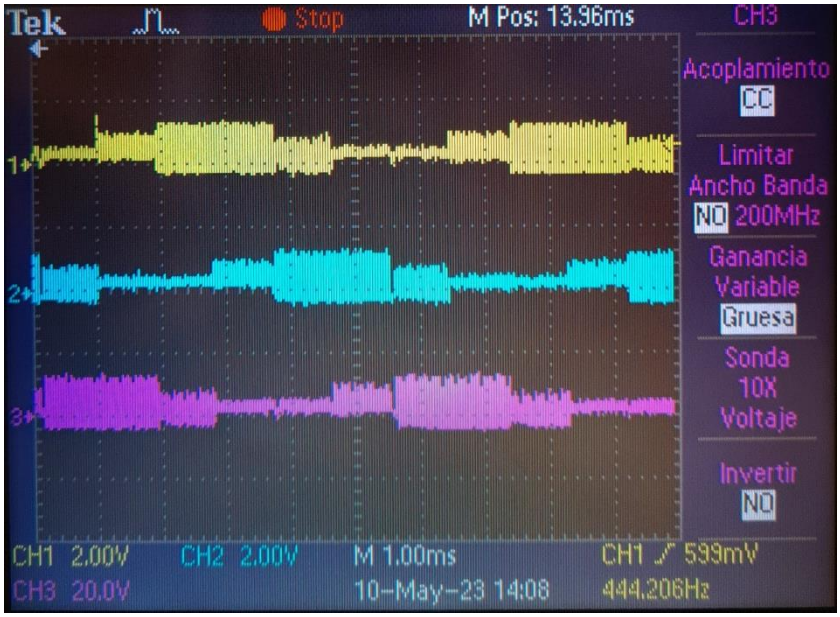

Figure 5.7 BEMF signals obtain from the motor. (Source: own)

These three BEMF signals correspond to phase A, B and C from top to bottom, and as can be seen, three parts can be distinguished in each phase signal.

In order to have a better analysis from this BEMF signals, the following figure has all signals refer to phase A. Thus, the BEMF signal can be compared with the signals supplied to the motor.

From the next picture, the yellow wave corresponds to the driver input signal, the blue wave is the BEMF signal, and the pink wave is the MOSFET enable signal. This electrical cycle

period of the signals shows the relationship between the two signals supplied to the motor and the generated BEMF waveform.

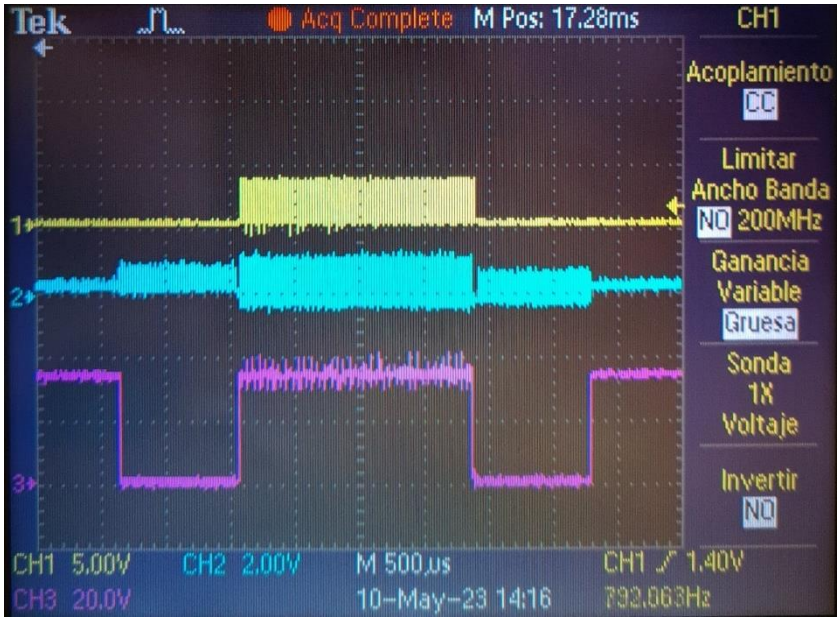

Figure 5.8 One electrical cycle period with all A-phase signals. (Source: own)

On the one hand, when the enable signal is high voltage, the BEMF gives the same signal but with some noise added, especially on 0 volts. This is because the conductors of the motor coils are connected at the common point, and a summation is generated between the two enabled phases of the motor.

On the other hand, when the enable signal is low are the states in which the MOSFETs of this phase are disabled, and it is at that moment when the zero crossing occurs. These states are also called high impedance states.

Afterwards, we tried to use another oscilloscope to see if we obtained a different signal quality and we obtained the following figure. Where the BEMF signal appears and below the motor input signal.

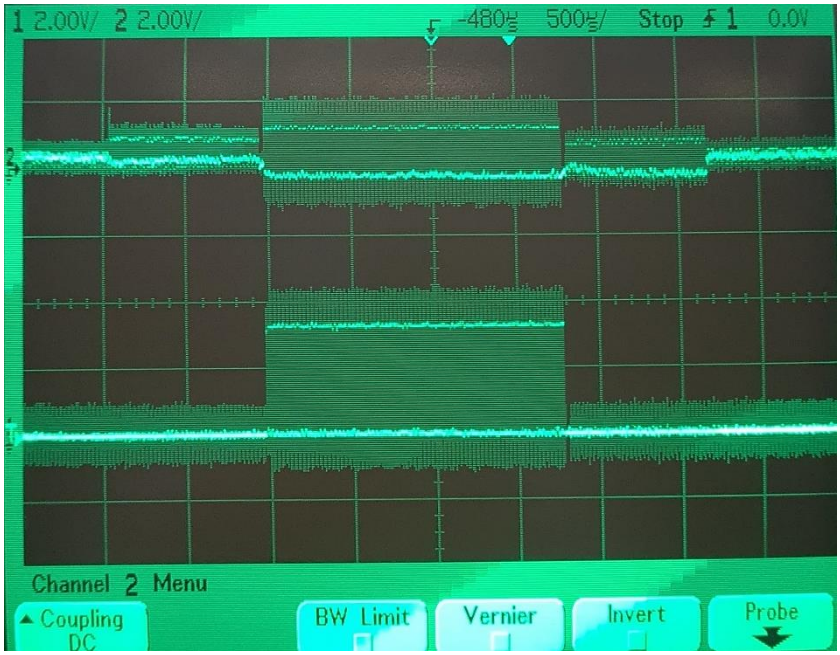

Figure 5.9 An electrical cycle period with two A-phase signals, Agilent oscilloscope. (Source: own)

Although there is approximately the same noise, on that oscilloscope the two parts of the PWM of the carrier signal could be differentiated.

To see these PWM time periods more clearly, the following image shows enlarged the previous signals, and the two values that the carrier signal rises can be recognized.

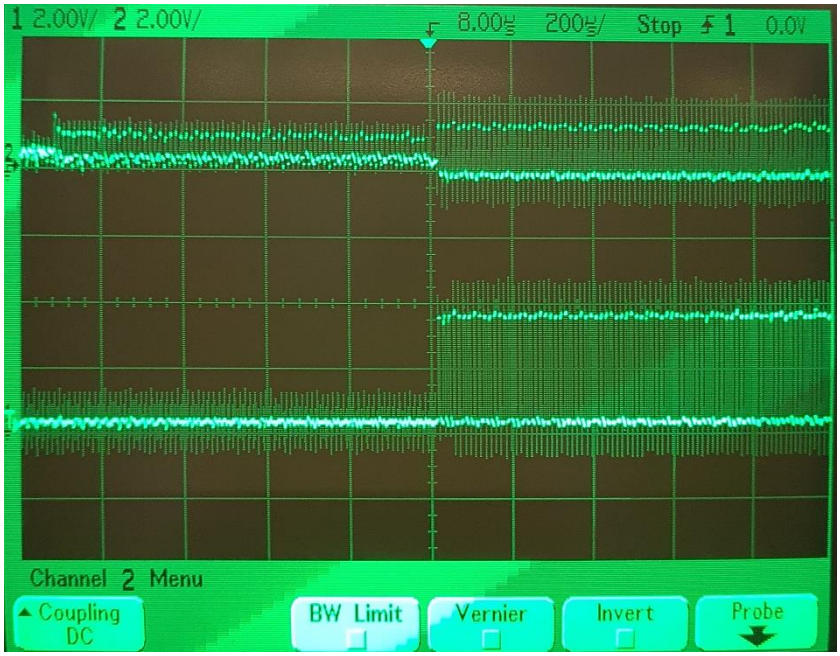

Figure 5.10 Enlarged view of the two previous signals, Agilent oscilloscope. (Source: own)

Therefore, the next proposed option was to perform a measurement while the phase was off, in the period of the $T_{PWM\ OFF}$ to obtain various values of the BEMF slope. Since during the $T_{PWM\ OFF}$ of the carrier signal is the BEMF value needed to know when it crosses the zero-crossing value. This method is one of the methodologies listed in the STMicroelectronics documentation. [22]

However, due to the high computational cost and the upper limitation of the PWM width to be able to perform the measurement, this idea was rejected. Then comparing in some forums our results with other people who also use the BEMF method, it has been proved that they use lower frequencies and obtain signals without so much noise.

The next option chosen was to achieve the closed voltage loop with the Hall effect sensor method, since the implementation cost of this method is not too high, and simpler computational resources are required.

Taking into account the theoretical statements about the Hall effect sensors and their data sheet, it was necessary to fabricate a board with the electrical components needed to make them work.

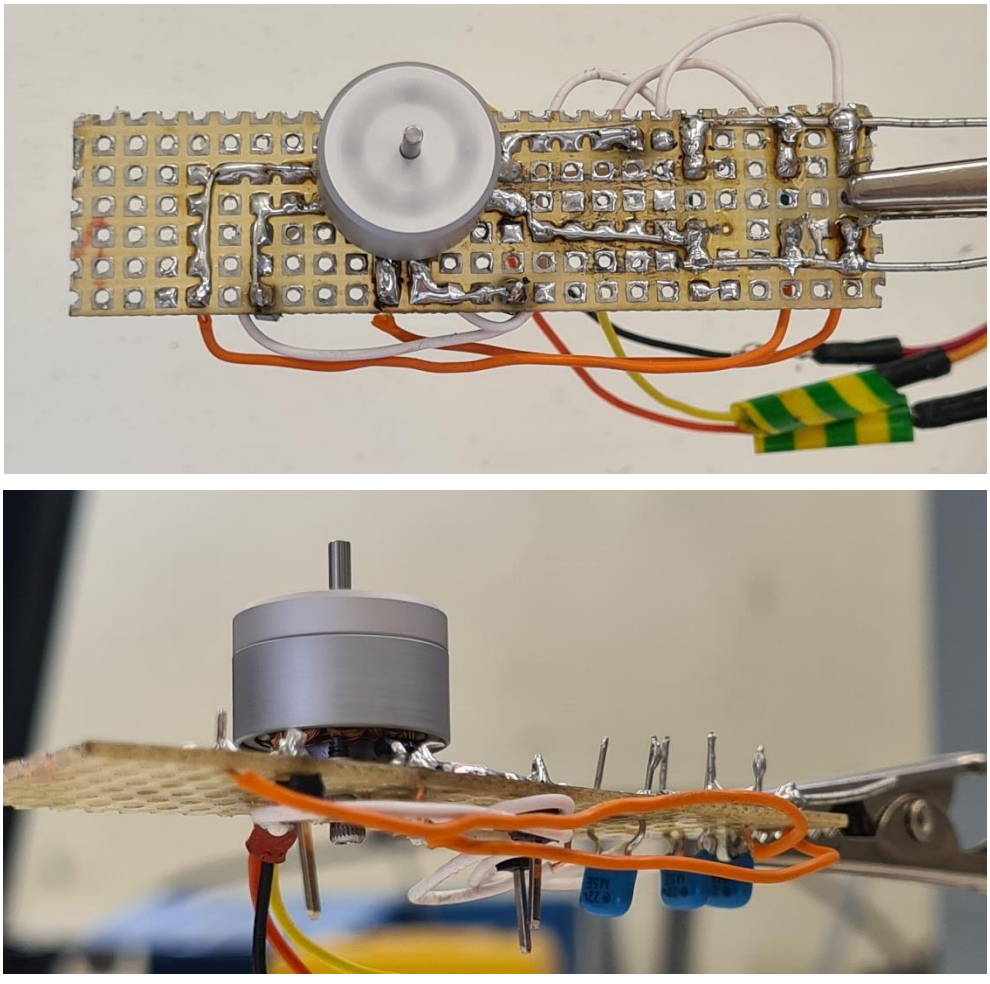

Figure 5.11 Prototype detection board for three Hall-effect sensors. (Source: own)

The placement of these small sensors is essential to detect the magnetic fields of the motor and consequently obtain the signals with the optimum state switching time. The following image shows the prototype board with the sensor placed with 120 electrical degrees between them.

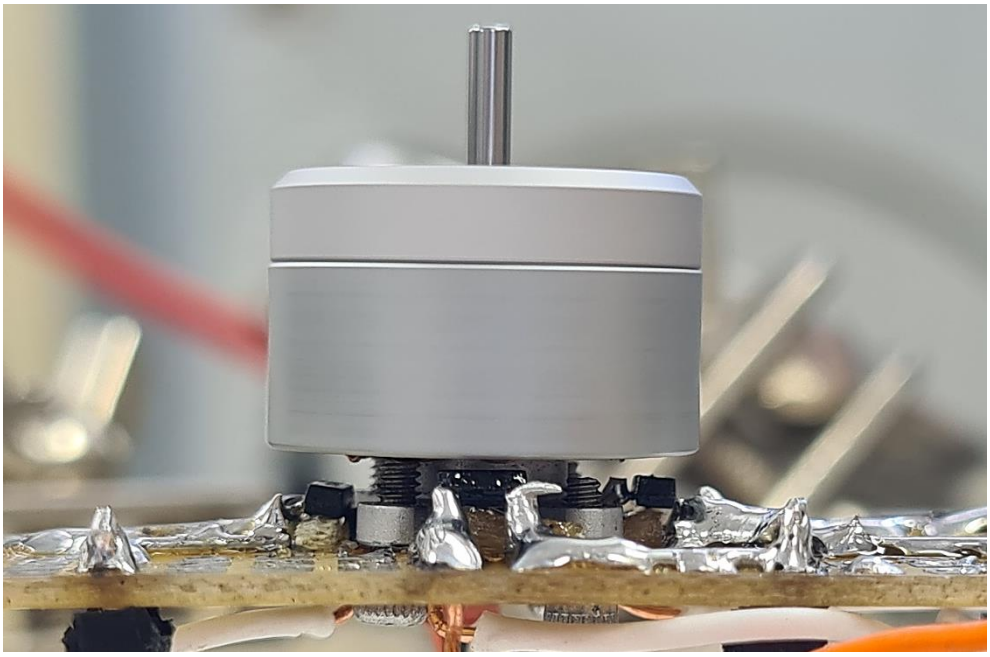

Figure 5.12 View of the placement of the sensors in relation to the motor. (Source: own)

After having the whole prototype assembled and running the motor in its open-loop control, a signal for each phase has been obtained.

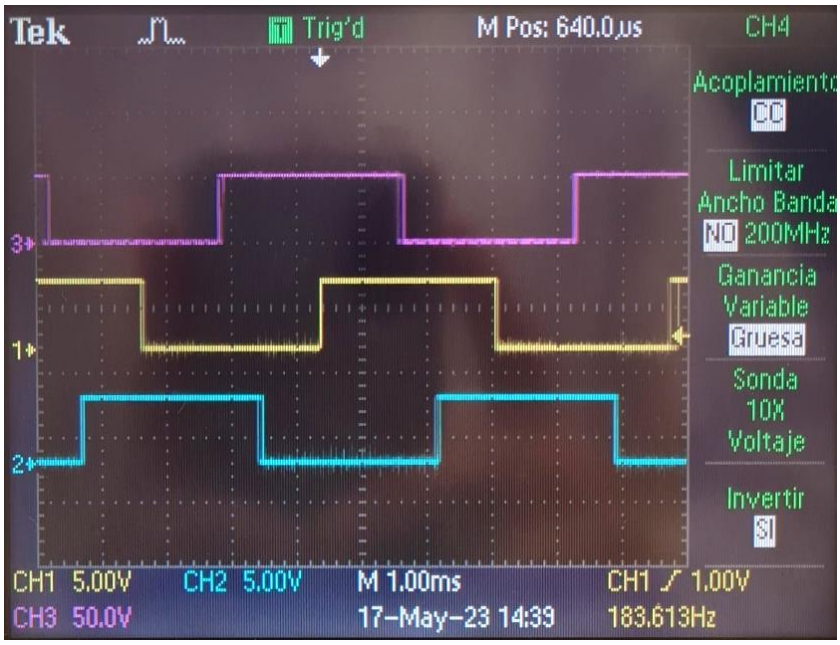

Figure 5.13 Sensor output signals obtained. (Source: own)

As can be seen the signals obtained are similar to the theoretical ones. Moving on to the next step, we code this part to read these signals from the sensors and change the state at the time they determine.

Once the code is ready just connect the output of the sensors to the driver and the closed loop voltage will have been achieved.

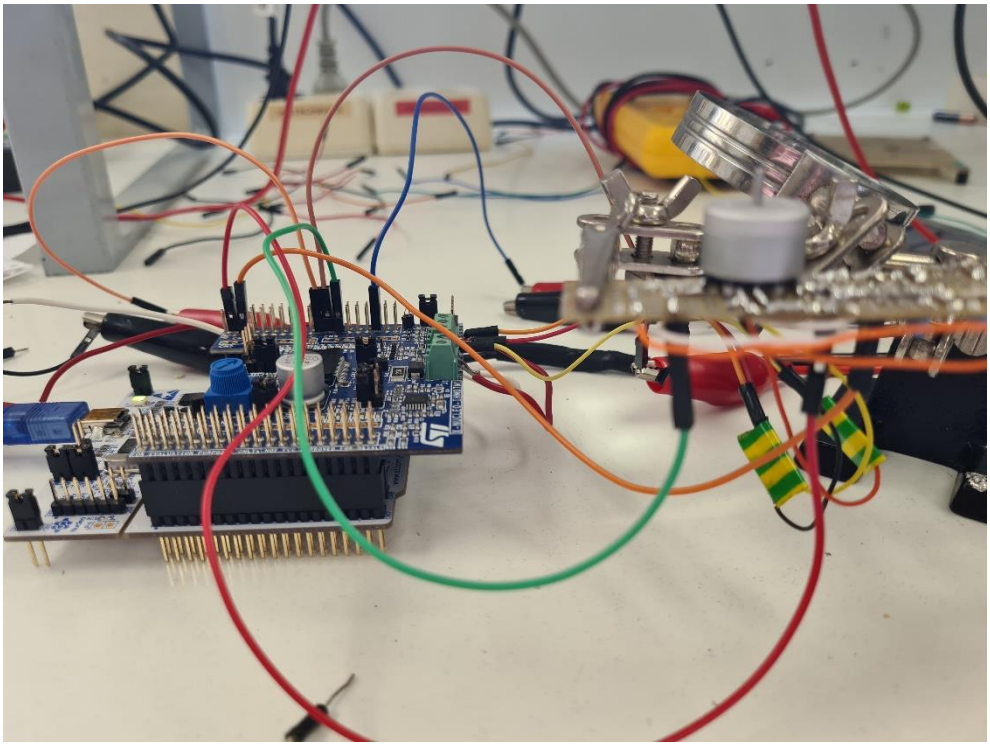

Figure 5.14 Second assembly with closed-loop tension control. (Source: own)

The operating results obtained are typical of closed-loop voltage control, where the rotational speed of the motor is directly dependent on the input voltage. Thus, when the motor input voltage increases, the motor rotation also increases, and vice versa.

In addition, unlike open-loop control, closed-loop control of the voltage performs well, since when some resistance is applied against the motor rotation the current consumption increases slightly to avoid motor stalling.

Nevertheless, if we look at the input signals for each phase, there is a different behavior from the previous ones.

The following image shows the three phases. These phases are ordered as phase A, phase C and phase B, from top to bottom. This definition of color is different from the one in the previous part of the thesis.

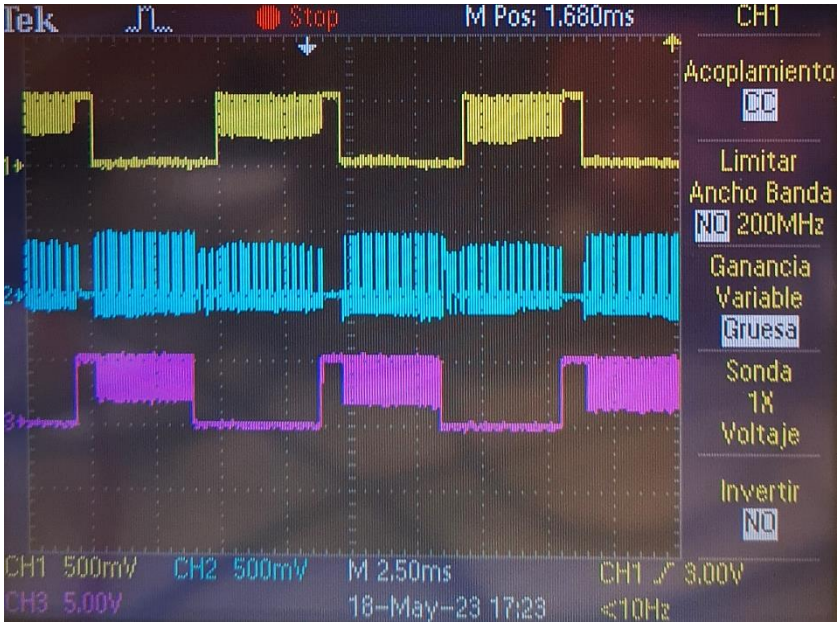

Figure 5.15 Representation of the problem in closed-loop input signals. (Source: own)

As can be seen, phase C does not work well since its signal is almost constant but in an unstable way. Moreover, the signals of phases A and B have some noise in a particular part of their waveform.

To have a different point of view, we use the other oscilloscope and by connecting to phase A and phase B the signal is displayed as follows.

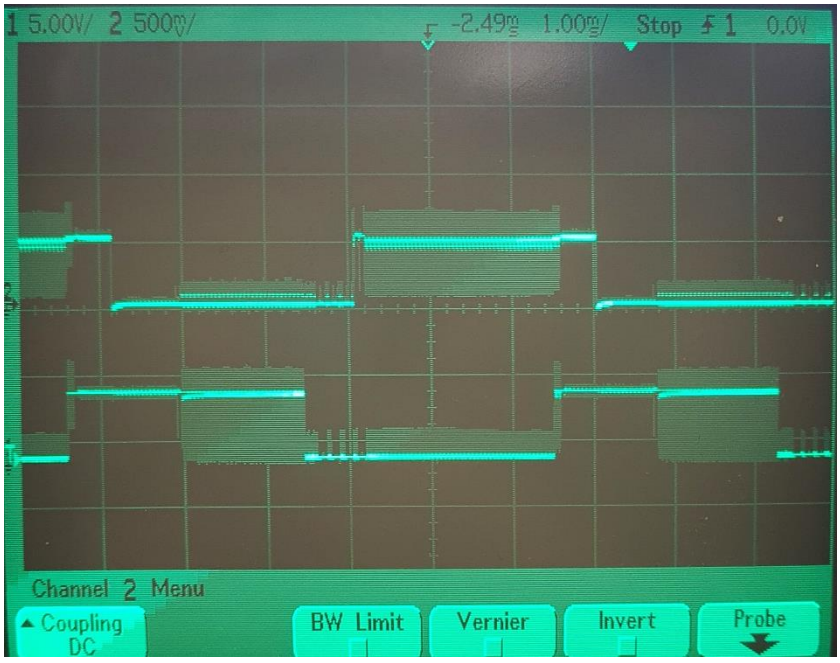

Figure 5.16 View of phase A and B signals, Agilent oscilloscope. (Source: own)

Then, phase B and phase C, respectively, were connected to the oscilloscope to obtain the following display.

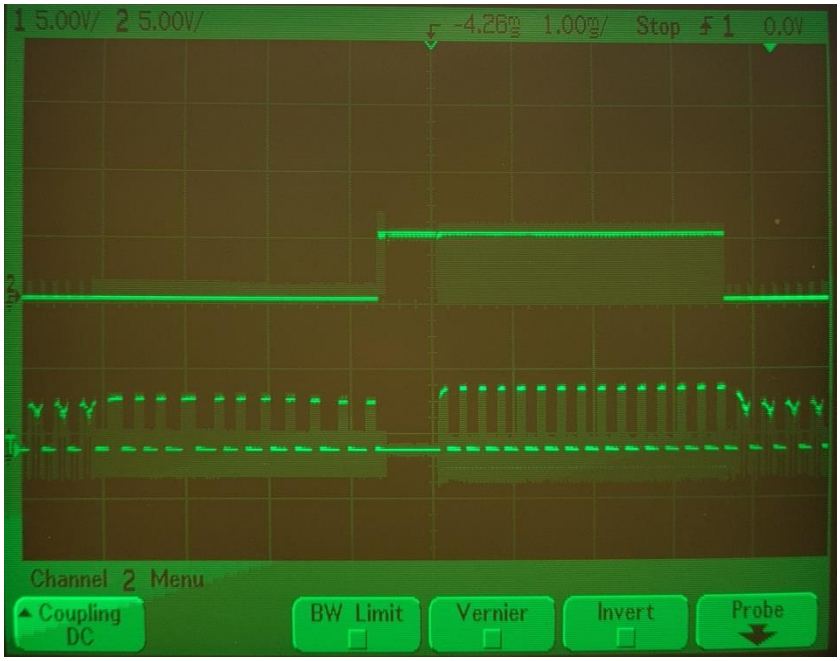

Figure 5.17 View of phase B and C signals, Agilent oscilloscope. (Source: own)

It seems that the switching between the different states was not working properly.

Afterwards, to discover the reason for this behavior, we went on to observe the signals of the Hall effect sensors. Since the operation of the code is based on changing the state when any sensor signal changes its value from 0v to high voltage or vice versa.

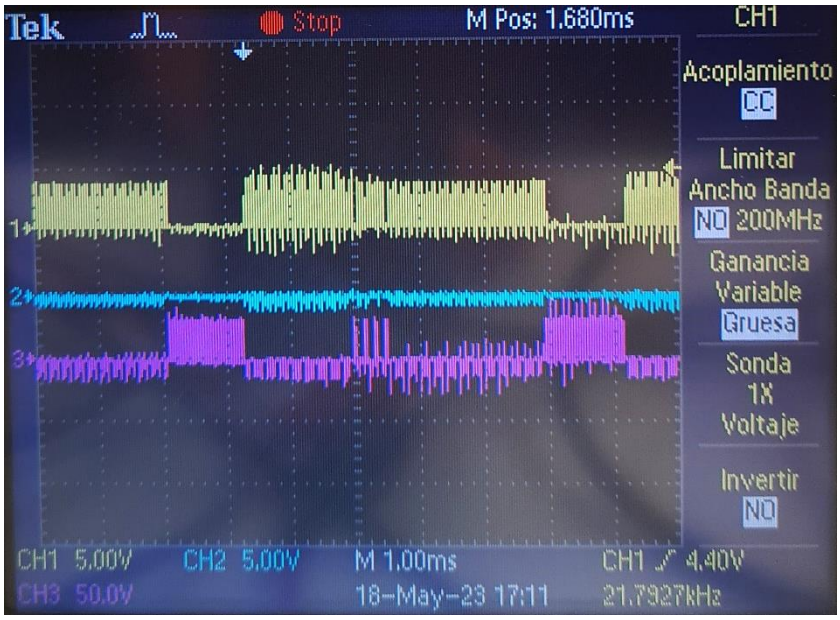

Figure 5.18 Representation of the problem in closed-loop sensor signals. (Source: own)

As is shown, the sensor signals have noise and there is a predominant situation where phase A is high and phase B is at 0v. This is why the code is supplying the wrong input signal to the motor even though the motor is still running.

In addition, we evaluated the behavior of the sensor signals with the same configuration but running the control code in open loop. Thus, we were able to find out whether the signal problem is due to the code or to the configuration.

Representing the motor input signals in this open-loop situation, the image is as follows.

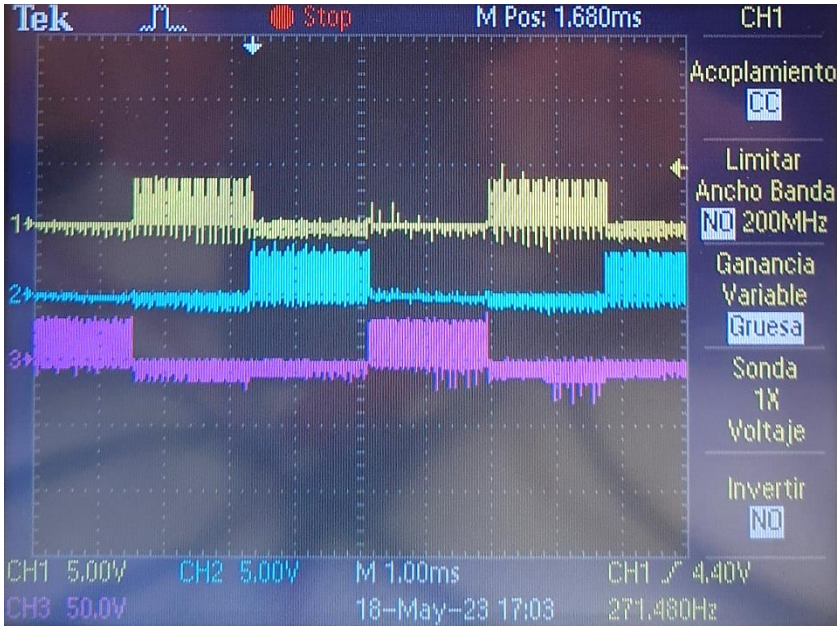

Figure 5.19 Representation of the problem in open-loop input signals. (Source: own)

As is shown, these signals have noise and some interferences, that if we compare these results with Figure 5.2 there is a non-continuity of the phases of the signals. While they should be the same signals as in Figure 5.2.

Therefore, the deduction that was made from this situation was that noise has been being coupled to the whole board, and it implies that on the sensor signals there is also this interference. It causes the code not to follow the required order of the states, and the code generates mainly some of the six states.

From this situation, some problems have been found, due to the small size of the motor and the low voltage and current used, the noise is more easily coupled as it usually has low values.

Furthermore, this configuration used to run the closed loop has a lot of connections made as cables that favors the appearance of noise. Besides, having so much frequency in the carrier signal generates that in the sensor waveform some extra noise is also added.

In order to reduce all these factors, the next step is to create a board with some filters on the sensor circuit battery and a low pass filter on each sensor output signal. In this way, it is possible to reduce the background noise and also eliminate excess wires.

Subsequently, the first part of the design process consists of drawing up a schematic of the connections that the board will have. The software to be used is KiCad EDA.

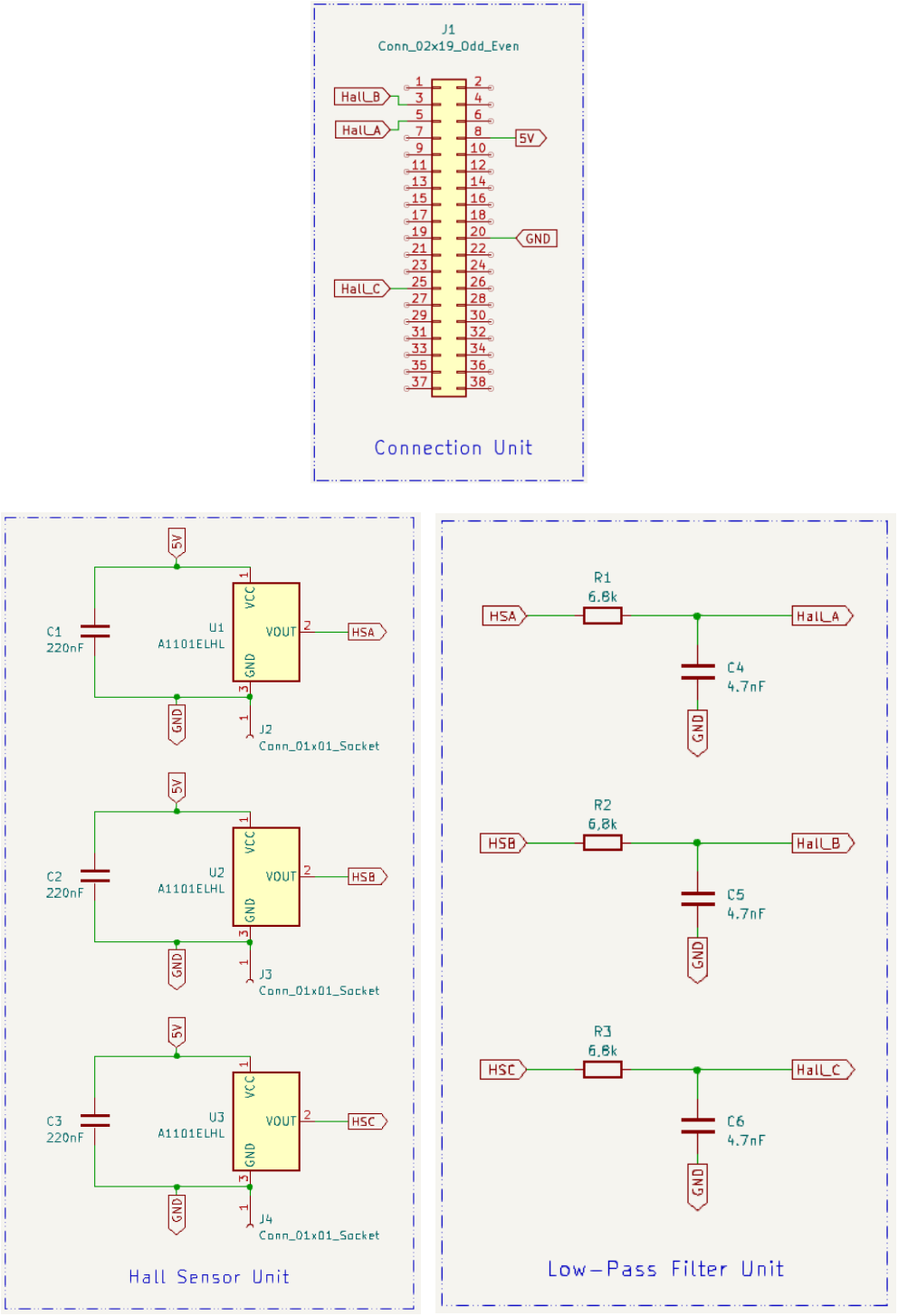

Figure 5.20 Circuit schematic for the implementation of Hall effect sensors. (Source: [31])

Once the schematic is ready, it is required to determine the dimensions of the board and the placement of the components that will go on it. In addition, the paths to connect the components are designed at the same time.

The result of the design is as follows.

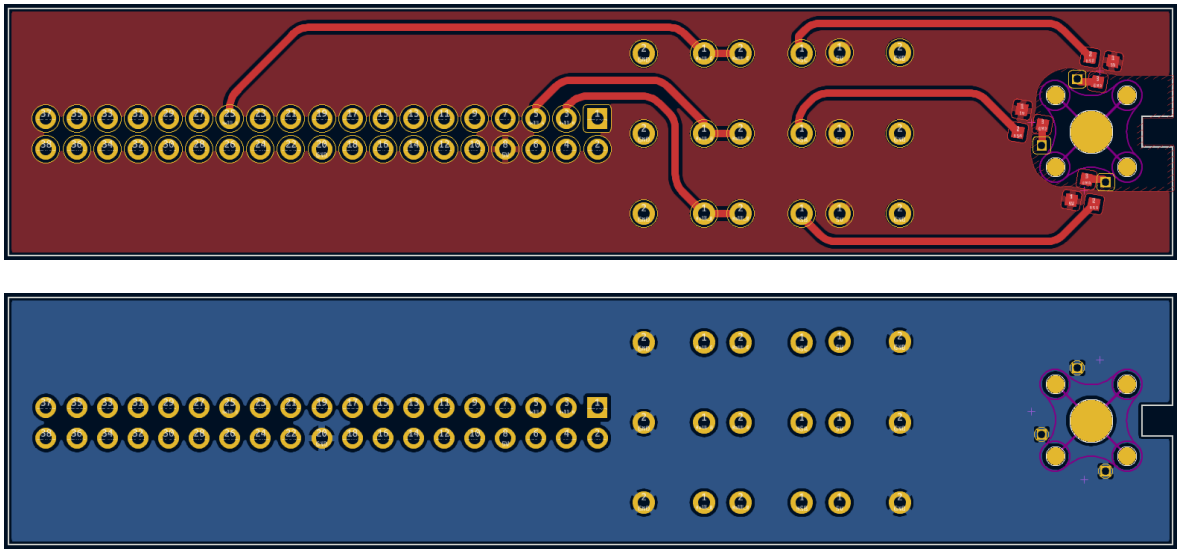

Figure 5.21 Two-dimensional representations of the sensor board and its electrical pathways. (Source: [31])

Mainly the idea of path distribution is the 5 volts supply and output sensor signals on the upper side, while on the bottom side there is the ground path of the whole circuit.

Then, the three-dimensional representation is as follows.

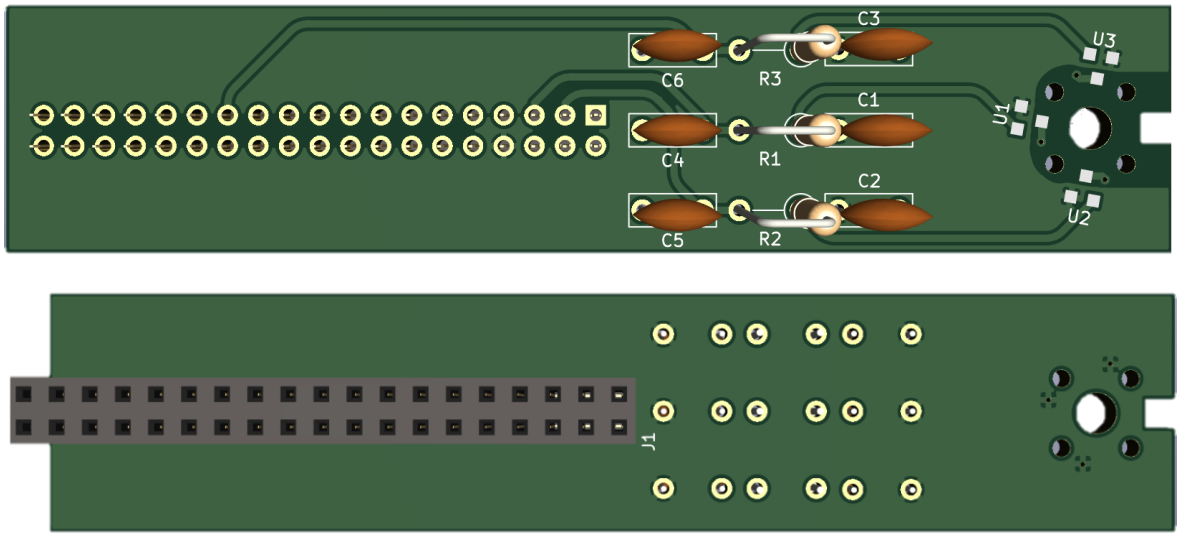

Figure 5.22 Three-dimensional representations of the sensor board and its electrical pathways. (Source: [31])

More specifically, the characteristic of the battery filters is that there are three 220 nanofarad capacitors and they should be located as close as possible to the sensors to optimize their performance. Moreover, the low pass filters at the sensor signal output are designed with a cutoff frequency around 5 KHz.

In addition, this board shape has been chosen to optimize space, the logical order of the components and to avoid the board coming into contact with other controller components.

Finally, the result of the PCB is as follows.

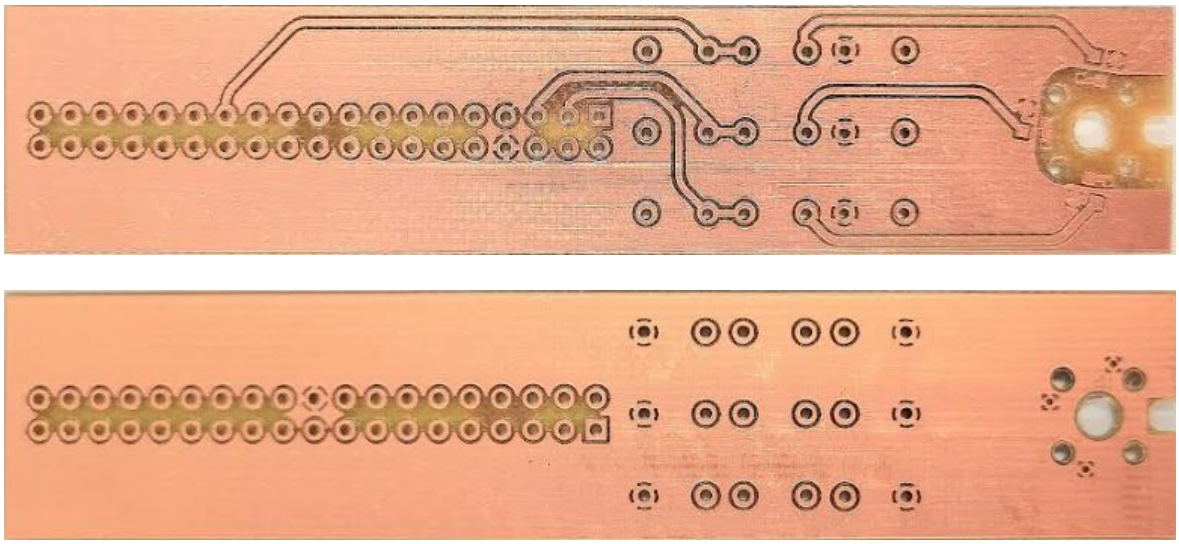

Figure 5.23 Fabricated printed circuit board. (Source: own)

After the electronical board printed is ready, the following step is to connect all the discrete components, but one line of capacitors is too close to the flywheel of the motor. For that reason, these capacitors will be connected on the bottom side of the board.

Once all the components have been soldered, and the Hall effect sensors have generated an acceptable signal, the board looks like the following image.

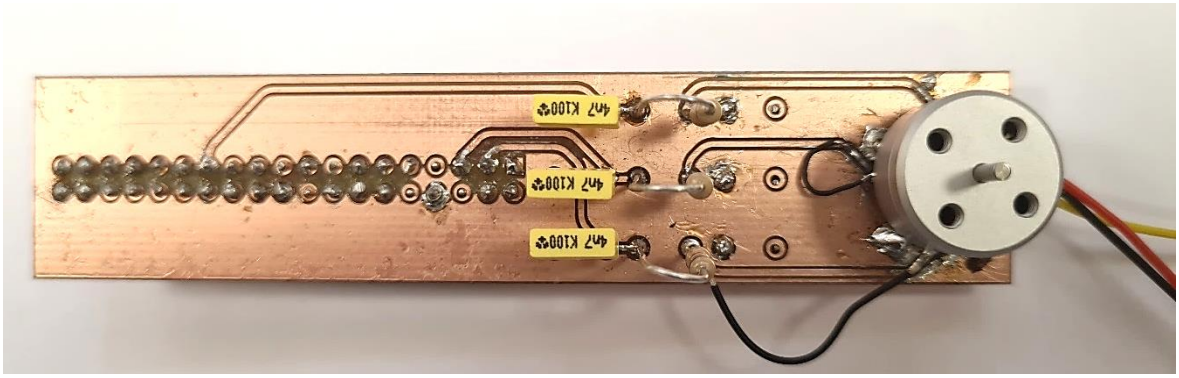

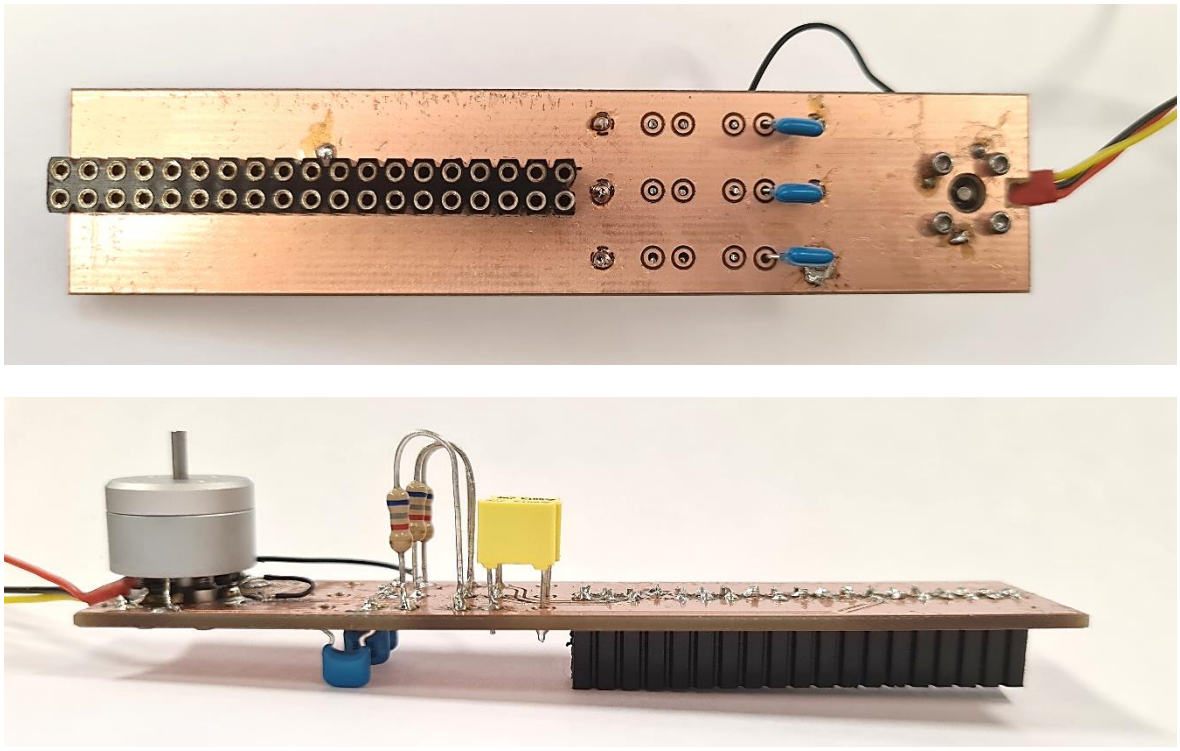

Figure 5.24 Final result of the PCB with the discrete components. (Source: own)

And the final assembly with the PCB of the Hall effect sensor is as follows.

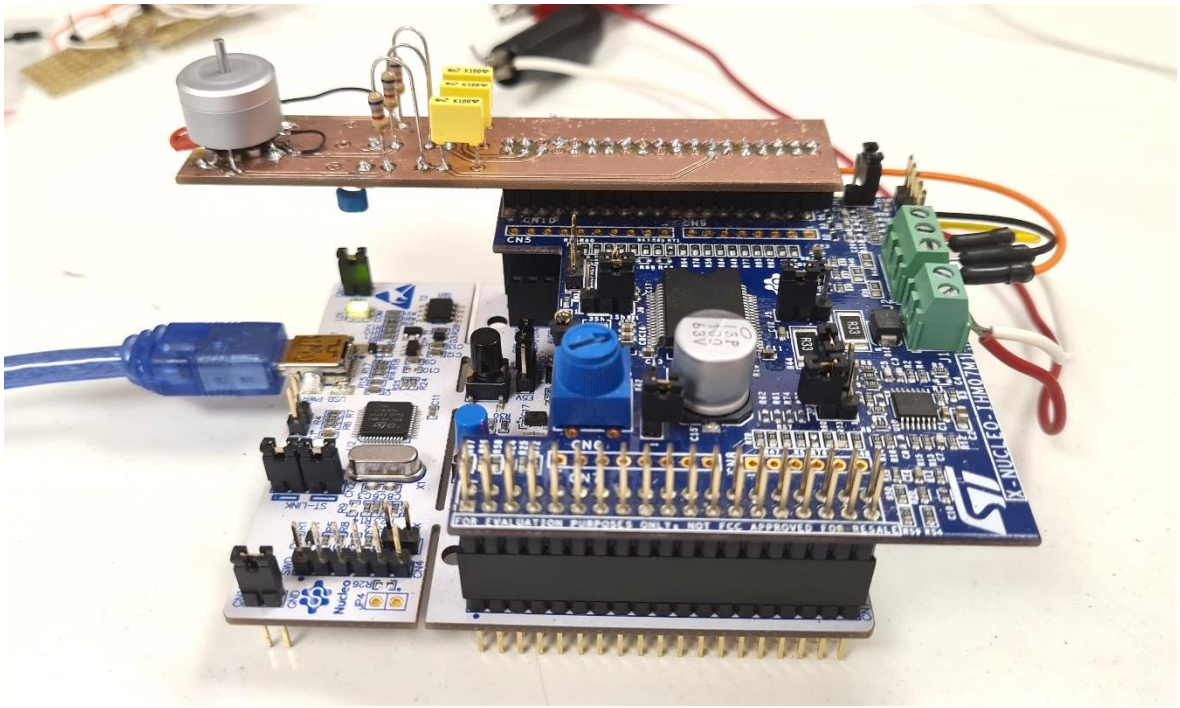

Figure 5.25 Final assembly with closed-loop tension control. (Source: own)

After obtaining the final assembly, the sensor signals must be adjusted by software. This is done in this way because the placement of the sensors is complex in cases where the motor has such small dimension. Particularly, their positions have had to be modified manually with respect to the design since they are far from detecting the magnetic field.

To make this adjustment of the sensors it is necessary to run the motor in open control loop and detect the BEMF signals of each phase. Then display the BEMF and the sensor signal of the same phase and thus calculates how much to delay or advance the sensor signals to match the approximate switching time.

This is determined by the BEMF, which is the signal that has the most accurate timing. First time only the calculation is made at a fixed speed to evaluate the operation of the motor.

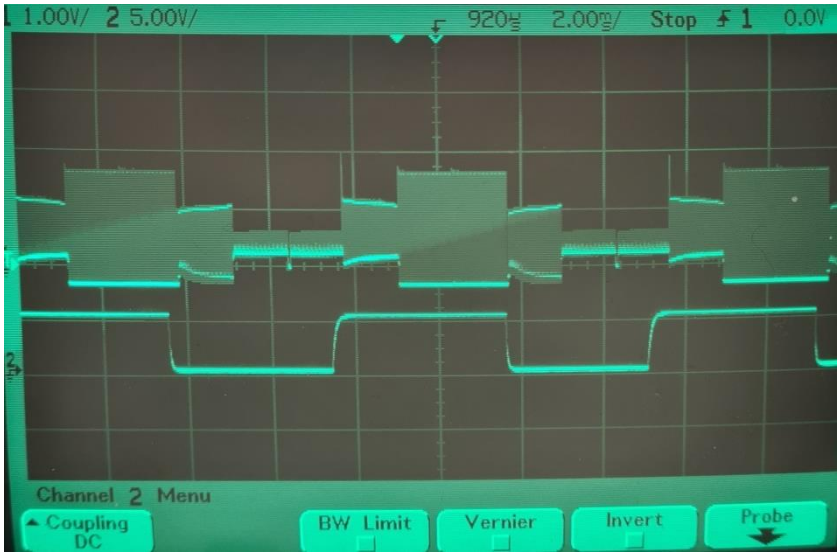

Figure 5.26 Experimental way to know the software delay or advance required. (Source: own)

As can be seen, there is a time lag between the BEMF and the sensor signal. In the case of this thesis all three signals are delayed with respect to the BEMF of their respective phase.

This situation of delaying the signals is easier than advancing them, so we just have to measure the time lag and add some code to wait for a period of time until the MOSFET state is switched.

Making all the calculation of each phase all the readjustment will be delaying the sensor signal and the following table is obtained.

Table 5.1 Readjustment of sensor signals. (Source: own)

Delaying for sensor signals		
Phase	Flank	Delay (µs)
A	↑	400
A	↓	600
B	↑	500
B	↓	400
C	↑	400
C	↓	500

Once it has been implemented, we analyze the input signals obtained by executing the closed-loop control.

As an additional comment, the signal from a sensor has a different amplitude. Its cause is that the driver has a circuit connected to this pin, and in order to measure the signal through this pin, jumper J3 must be opened to disconnect this internal circuit to this pin.

Therefore, the signal does not reach the maximum and minimum value like the other waveforms.

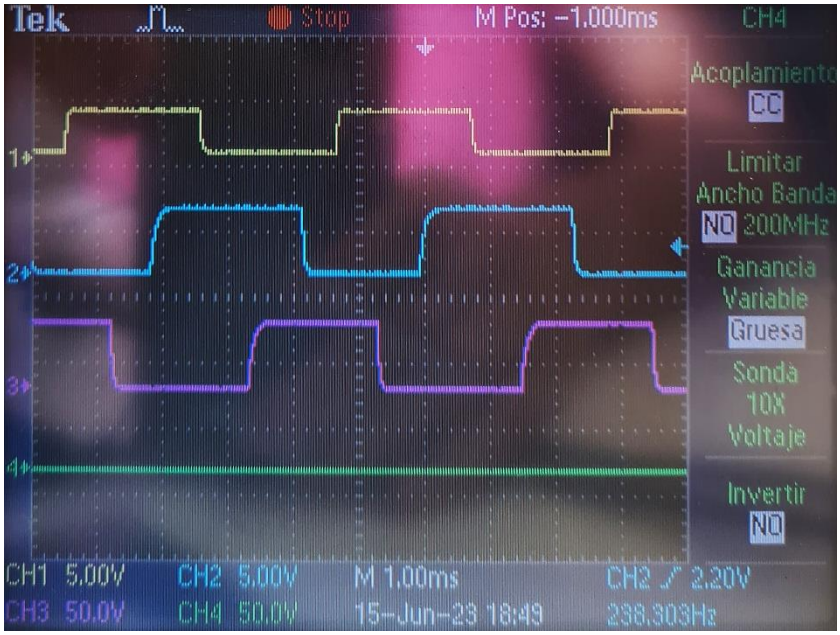

Figure 5.27 Phase A input signal and the three sensor waveforms. (Source: own)

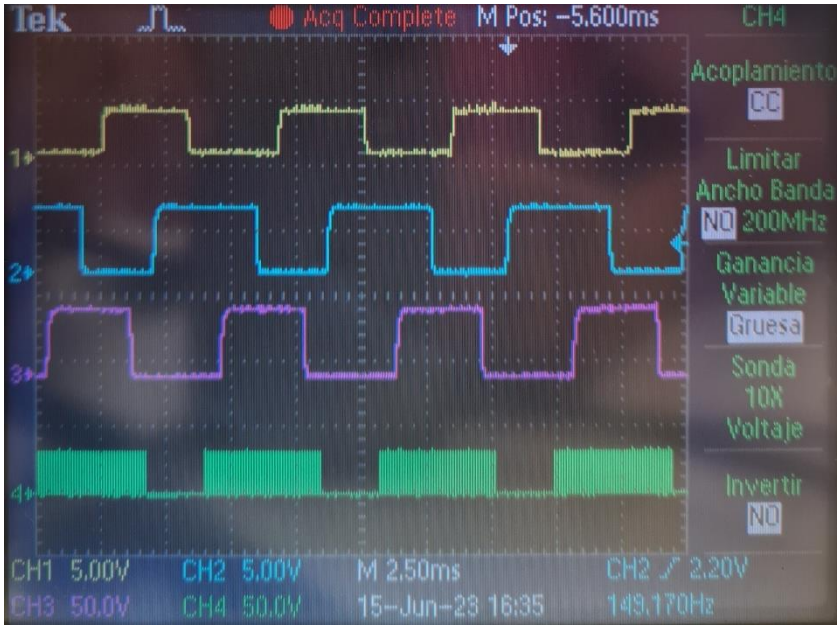

Figure 5.28 Phase B input signal and the three sensor waveforms. (Source: own)

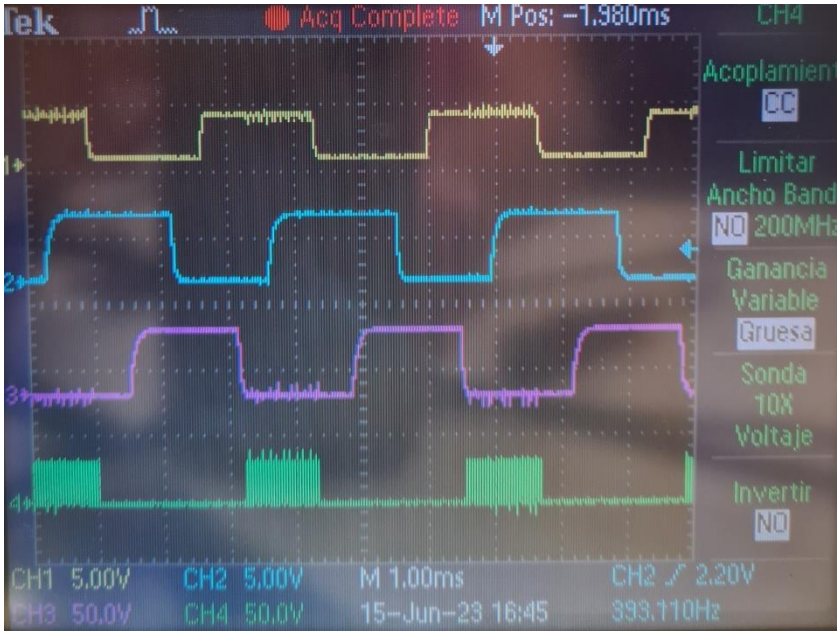

Figure 5.29 Phase C input signal and the three sensor waveforms. (Source: own)

First, the main objective of developing this PCB was to filter the sensor output signals and reduce the noise coupled. In that case both objectives have been achieved.

Then, although the time scale is not the same, two of these input phases from these previous figures are wrong. Since, each green phase signal of these pictures should be like the waveforms shown in Figure 5.2.

So, in phase A there is no signal, in phase B it seems to be twice as long as the signal should be activated, and then the last phase is the only one that seems to be right.

After searching for answers to this situation, some possibilities about the code emerged.

In this case of having a motor of reduced dimensions, the interruptions in the code must be short processes, maximum around 200µs, since it is the time between signal edges that will determine the switching state.

Otherwise, we will lose signal information because at the time an interrupt is executed the main program freezes, meanwhile the sensor signals never stop.

Therefore, the interrupt function should not have any delay or wait structure and should avoid calling external functions that will cause the interrupt to spend too much time.

The solution to this problem is to code the program as low-layer code. That means, we will replace functions like "digitalWrite()" by defining a binary number to a variable that the microcontroller will recognize.

Finally, the variations that we must take into account in the following steps is that the synchronization process of the sensor signals must be out of interrupt functions to avoid any loss of information. Moreover, the STMicroelectronics pins have some incompatibilities with Arduino, so it will be necessary to download some extra libraries.

The libraries we recommend are the following. [32]

And the documentation for finding support for low-layer coding is as follows. [33]

6 Budget

The purpose of the following section is to summarize the overall budget required to realize this thesis, considering the components, software and personal time invested.

On the one hand, all the components used in this thesis to achieve the attitude control of the brushless motor are listed in the following table.

The prices of these components could vary depending on the shopping site.

Table 6.1 Budget for electrical devices. (Source: own)

Electrical devices				
Item	Quantity	Unity price (€)	Total price (€)	Shopping site
BLDC motor EMAX 1104 4300K	1	2,17	2,17	[25]
Microcontroller Nucleo F411RE	1	15,17	15,17	[34]
Driver X-Nucleo-IHM07M1	1	11,91	11,91	[24]
TOTAL			**29,25**	

Next, the flywheel that will go on the rotor of the motor is made on the UPC 3D printer, as it is also a prototype. UPC Terrassa has some of its services at people's disposal and anyone can contact them to use it.

Table 6.2 Budget for reaction wheel. (Source: own)

Reaction wheel				
Item	Quantity	Unity price (€)	Total price (€)	Shopping site
Reaction wheel	1	0,00	0,00	[26]
TOTAL			**0,00**	

Afterwards, for the PCB required in this thesis, it has been manufactured with milling machine at UPC Terrassa and then the components have been soldered. Therefore, the budget for the PCB part is as follows.

Table 6.3 Budget for PCB. (Source: own)

PCB				
Item	Quantity	Unity price (€)	Total price (€)	Shopping site
Capacitors 220nF	3	0,66	1,98	[35]
Capacitors 4,7nF	3	0,49	1,47	[36]
Resistance 6,8kΩ	3	0,18	0,54	[37]
Hall effect sensor SOT-23 AH372-SA-7	3	0,30	0,90	[38]
Winslow multiple base 38 ways in 2 rows	1	1,26	1,26	[39]
Copper Plate for PCB, AE16, Double Sided	1	7,42	7,42	[40]
TOTAL			**13,57**	

In this PCB budget the prices are referred to buy the minimum package of each component, which can be from 5 to 10 components.

As for the software used in the project, both are free of charge.

Table 6.4 Budget for software licenses. (Source: own)

Software licenses				
Item	Quantity	Unity price (€)	Total price (€)	Shopping site
Arduino IDE	1	0,00	0,00	[1]
KiCad EDA	1	0,00	0,00	[31]
TOTAL			**0,00**	

Finally, the last part to be included in the total budget will be the personal dedication to this project. Additionally, as can be seen in Table 5.1 and Figure 5.1, the duration of the work packages is explained. So, if the average number of hours invested each day is around 3 hours and as the time available is 19 weeks, the final number of hours is 399 hours.

In addition, to determine the price per hour to the personal dedication we search on Generalitat web page, where determine that professional Scientific and intellectual professionals has a price per hour around 25,28 €. [41]

Table 6.5 Budget for personal dedication. (Source: own)

Personal dedication				
Item	Quantity (h)	Price per hour (€)	Total price (€)	Information site
Persona dedication	399	25,28	10.086,72	[41]
TOTAL			**10.086,72**	

Afterwards, considering all the different budgets of this thesis, the following total budget is obtained.

Table 6.6 Total budget. (Source: own)

Total budget	
Item	Total price (€)
Electrical devices	29,25
Reaction wheel	0,00
PCB	13,57
Software licenses	0,00
Persona dedication	10.086,72
TOTAL	**10.128,54**

Considering that the production cost will be only the summation of the electrical devices budget and the PCB budget, the total cost of the attitude control is 42,82€ which is around 15% of the Maxon attitude control price. It can be compared with Alev Yilmaz thesis where its hardware budget was around 300€. [4]

7 Conclusions

7.1 Reflection on the thesis

To conclude, the first objective of changing the brushed motor is achieved, as an attitude control design for a brushless motor is obtained. And this variation will result in improved efficiency and reduced vibration compared to the MAXON motor.

On the other hand, at the beginning of this thesis there is the other requirement of reducing the cost of attitude control proposed by Alev Yilmaz. Therefore, as can be seen from the budget, the total cost of the components and boards results to be approximately 15% of the price of the MAXON attitude control hardware. A statement that makes the implementation on a CubeSat more affordable.

However, currently the BLDC motor of this thesis is not as functional as the MAXON engine. So, more research hours need to be invested in attitude control from BLDC motors.

Then, regarding the motor speed control and the decisions that have been made are satisfactory. Since, due to the limited dimensions of this BLDC motor, a closed voltage loop has been implemented from the Hall effect sensor. In addition, all the variations made in this thesis have a substantiated and documented cause that makes the direction of the project has been changeable.

Finally, it is worth mentioning that one point of the thesis scope has not been achieved because the attitude control assembly of this thesis has not been optimized, so it has not been installed it in the CubeSat.

7.2 Areas for improvement

Afterwards, this section will mention some recommendations and areas for improvement considering the documentation of this project and the point of view of people who has carried it through all its phases.

- The coding in lower layers to obtain the best available performance of the microcontroller and make it capable of controlling the brushless motor of such reduced dimensions. And all this without problems of loss of information from any sensor and optimizing the operation of the microcontroller.

  In addition, it will be important to be aware of the lack of compatibility between STM32 boards and low layer Arduino coding. Therefore, it will be necessary to download some free libraries.

- Once the above recommendation has been made, it is assumed that the input signals will be approximately correct, although it will be necessary to synchronize the sensor signals by software. However, it will have to be in a more general way than what has been done in this thesis, since the period of the signals will depend on the actual motor speed, and the delay or advance process will vary.

- In addition, a change of the microcontroller board could be adequate to reduce the cost, since no such amount of memory is needed to run this code and the dimensions will be better to locate this module to the future CubeSat.

- By the same way, the design of a new driver, including the hall-effect sensor developed in this thesis, could lead to improved optimization and suitability to the needs. Since at least three reaction wheels would be required in the future CubeSat, the design of the new driver should have three voltage supplies for the motors and the same number of Hall effect sensor circuits to measure their switching momentum.

  Furthermore, future versions of the designed printed circuit board should take into account the height required by the Hall effect sensors to obtain greater accuracy.

- Finally, the last recommendation to improve attitude control is to design a new closed loop but this time current based and implement PID control. This will allow more precise torque control and the desired speed will be achieved in a controlled manner.

8 References

[1] «Software». https://www.arduino.cc/en/software (consulta 12 juny 2023).

[2] «STMicroelectronics: Our technology starts with you». https://www.st.com/content/st_com/en.html (consulta 17 març 2023).

[3] J. Serrano Aporta, «Attitude control techniques for a 1U CubeSat», Bachelor thesis, Universitat Politècnica de Catalunya, 2022. Consulta: 15 març 2023. [En línia]. Disponible a: https://upcommons.upc.edu/handle/2117/372841

[4] A. Yilmaz, «Programming the attitude control of a CubeSat for simulation of LEO orbit space missions», Bachelor thesis, Universitat Politècnica de Catalunya, 2023. Consulta: 19 juny 2023. [En línia]. Disponible a: https://upcommons.upc.edu/handle/2117/386241

[5] A. Space, «A Basic Guide to Nanosatellites», *Alén Space*. https://alen.space/basic-guide-nanosatellites/ (consulta 24 març 2023).

[6] A. Pérez Portero, «Design, implementation and verification of CubeSat systems for Earth Observation», Master thesis, Universitat Politècnica de Catalunya, 2019. Consulta: 23 març 2023. [En línia]. Disponible a: https://upcommons.upc.edu/handle/2117/134850

[7] «Industria Espacial | SpaceRobotics.eu», 27 març 2018. https://www.spacerobotics.eu/industria-espacial/ (consulta 21 abril 2023).

[8] J. J. Wijker, *Spacecraft Structures*. Springer Science & Business Media, 2008.

[9] «Gen-1-SENSORS-ACTUATORS-Jan-2023-web.pdf». Consulta: 3 juny 2023. [En línia]. Disponible a: https://www.cubesatshop.com/wp-content/uploads/2023/05/Gen-1-SENSORS-ACTUATORS-Jan-2023-web.pdf

[10] «ADCS: Attitude Determination And Control System - ECE3SAT». http://www.ece3sat.com/cubesatmodules/adcs/ (consulta 22 abril 2023).

[11] J. Zhang i Y. Qiang, «Project of 1DoF attitude control system of 1U cubesat based on reaction wheel», Bachelor thesis, Universitat Politècnica de Catalunya, 2021. Consulta: 23 març 2023. [En línia]. Disponible a: https://upcommons.upc.edu/handle/2117/360612

[12] M. Duran i A. Eloisa, «Design and manufacture of 3DOF reaction wheels as actuators for attitude control of a 1U CubeSat», Master thesis, Universitat Politècnica de Catalunya, 2022. Consulta: 23 març 2023. [En línia]. Disponible a: https://upcommons.upc.edu/handle/2117/374974

[13] «L3G4200D MEMS Motion Sensor Ultra-Stable 3-Axis Gyroscope I2C Mini Module», *store.ncd.io*. https://store.ncd.io/product/l3g4200d-mems-motion-sensor-ultra-stable-3-axis-gyroscope-i2c-mini-module/ (consulta 3 juny 2023).

[14] «MAUS (drw-nr: 114T000) - Radiation hardened cubesat Sunsensor», *Lens Research and Development*. https://lens-rnd.com/sun-sensors/maus-sun-sensor/ (consulta 3 juny 2023).

[15] «Magnetic Sensor - 1108_0 at Phidgets». https://www.phidgets.com/?tier=3&catid=5&pcid=3&prodid=78 (consulta 3 juny 2023).

[16] «Gen 1: CubeSense», *CubeSatShop.com*. https://www.cubesatshop.com/product/gen-1-cubesense/ (consulta 3 juny 2023).

[17] «Digital Earth Sensor - Earth/Horizon Sensor | SatCatalog». https://www.satcatalog.com/component/digital-earth-sensor/ (consulta 3 juny 2023).

[18] «NSS CubeSat ACS solution», *CubeSatShop.com*. https://www.cubesatshop.com/product/cubesat-acs-board/ (consulta 3 juny 2023).

[19] «Reaction wheels on the global market», *satsearch blog*, 25 juliol 2019. https://blog.satsearch.co/2019-07-25-reaction-wheels-an-overview-of-attitude-control-systems-available-on-the-global-marketplace-for-space (consulta 3 juny 2023).

[20] L. / News, «Morpheus thruster propels single cubesat to lower orbit», *LaptrinhX / News*, 23 juliol 2020. https://laptrinhx.com/news/morpheus-thruster-propels-single-cubesat-to-lower-orbit-N9oxNg5/ (consulta 3 juny 2023).

[21] «Sensorless brushless DC motor - an explanation». https://owenduffy.net/rc/BLDC/index.htm (consulta 28 maig 2023).

[22] «Sensorless BLDC motor control and BEMF sampling methods with ST7MC».

[23] «NUCLEO-F411RE - STM32 Nucleo-64 development board with STM32F411RE MCU, supports Arduino and ST morpho connectivity - STMicroelectronics». https://www.st.com/en/evaluation-tools/nucleo-f411re.html (consulta 12 juny 2023).

[24] «X-NUCLEO-IHM07M1 - Three-phase brushless DC motor driver expansion board based on L6230 for STM32 Nucleo - STMicroelectronics». https://www.st.com/en/ecosystems/x-nucleo-ihm07m1.html (consulta 12 juny 2023).

[25] «EMAX-motor sin escobillas para Dron de carreras, cuadricóptero de control remoto, 1103, 1105, 1106, 1104, 4300KV, 2-4S, 2-3 pulgadas, FPV, BabyHawk KINGKONG 2345 AVAN 2,3 - AliExpress Juguetes y pasatiempos». https://es.aliexpress.com/i/1005002190328136.html?gatewayAdapt=glo2esp (consulta 12 juny 2023).

[26] admin, «Català», *UPCFAB Terrassa*. https://upcfabterrassa.upc.edu/ca (consulta 18 juny 2023).

[27] PROMAX, «FA-665B: Fuente de laboratorio doble 2x30V,5A (auxiliar 5V,3A) | PROMAX». https://www.promax.es/esp/productos/fuentes-alimentacion-laboratorio-regulables/FA-665B/fuente-laboratorio-doble-2x30v-5a-auxiliar-5v-3a/ (consulta 20 juny 2023).

[28] «Tektronix, TDS2024B». https://www.sglabs.it/en/product.php?s=tektronix-tds2024b&id=1563 (consulta 13 juny 2023).

[29] «Osciloscopio de señal mixta digital Agilent 54622D laboratorio», *eBay*. https://www.ebay.es/itm/266292501915 (consulta 13 juny 2023).

[30] «31.79€ 25% de DESCUENTO|Eruntop Estación de soldadura 8586, soldador eléctrico con pantalla Digital, pistola de calor de aire caliente, máquina de soldadura para reparación de iPhone|soldering iron|station hot air gunrework station - AliExpress», *aliexpress.com*. //es.aliexpress.com/item/2024661747.html?src=ibdm_d03p0558e02r02&sk=&aff_platform=&aff_trace_key=&af=&cv=&cn=&dp= (consulta 20 juny 2023).

[31] «KiCad EDA». https://www.kicad.org/ (consulta 11 juny 2023).

[32] «Arduino core support for STM32 based boards». STM32duino, 19 juny 2023. Consulta: 19 juny 2023. [En línia]. Disponible a: https://github.com/stm32duino/Arduino_Core_STM32

[33] «CD00171190-.pdf». Consulta: 19 juny 2023. [En línia]. Disponible a: https://www.st.com/resource/en/reference_manual/CD00171190-.pdf

[34] «NUCLEO-F411RE | Placa de desarrollo STM32 Nucleo-64 de STMicroelectronics, con núcleo ARM Cortex M4F | RS». https://es.rs-online.com/web/p/kits-de-desarrollo-de-microcontroladores/8224052?redirect-relevancy-data=7365617263685F636173636164655F6F726465723D31267365617263685F696E746572666163655F6E616D653D4931384E536561726368476 56E65726963267365617263685F6D617463685F6D6F64653D6D61746368616C6C7061727469616C267365617263685F7061747465726E5F6D6174636865643D5E5B5C707B4C7D5C707B4E647D2D2C2F255C2E5D2B24267365617263685F747970653D4B4559574F52445F53494E474C455F414C5048415F4E554D4552494326736561726368 5F7370656C6C5F636F72726563745F6170706C6965643D59267365617263685F77696C645F63617264696E675F6D6F64653D4E4F4E4526736561726368 5F6B6579776F72643D4E55434C454F2D4634313152452673656172632 63685F6B6579776F72645F6170703D4E55434C454F2D46343131524526 (consulta 18 juny 2023).

[35] «MKS4D032202B00KF00 | Condensador de película WIMA, 220nF, ±10%, 63 V ac, 100 V dc, Montaje en orificio pasante | RS». https://es.rs-online.com/web/p/condensadores-de-pelicula/1082750 (consulta 18 juny 2023).

[36] «F472K75Y5RN83K0R | Condensador cerámico monocapa (SLCC) Vishay, 4.7nF, ±10%, 1kV dc, Montaje en orificio pasante, Y5R dieléctrico | RS». https://es.rs-online.com/web/p/condensadores-ceramicos/6832134 (consulta 18 juny 2023).

[37] «ROX1SJ6K8 | Resistencia TE Connectivity, de 6.8kΩ ±5%, 1W, Serie ROX1S | RS». https://es.rs-online.com/web/p/resistencias-de-montaje-en-orificio-pasante/2141254 (consulta 18 juny 2023).

[38] «Sensor de efecto Hall, AH372-SA-7, SOT-23 3 pines Sensores de efecto Hall | RS». https://es.rs-online.com/web/p/circuitos-integrados-de-sensores-de-movimiento/1333330 (consulta 18 juny 2023).

[39] «W35532TRC | Base múltiple Winslow, de 32 vías en 1 fila, paso 2.54mm, 12A, , montaje orificio pasante, para soldar | RS». https://es.rs-online.com/web/p/conectores-hembra-para-pcb/2677416 (consulta 18 juny 2023).

[40] «Placa de Cobre para PCB, AE16, Doble Cara, Base FR4, FR4, grosor 35µm, 100 x 160 x 1.6mm | RS». https://es.rs-online.com/web/p/placas-de-cobre-para-pcb/2192139 (consulta 18 juny 2023).

[41] «Idescat. Anuario estadístico de Cataluña. Salario bruto anual y ganancia por hora. Por sexo y tipo de empleo.» https://www.idescat.cat/indicadors/?id=aec&n=15376&lang=es (consulta 18 juny 2023).